



## Effect of deformation on helium storage and diffusion in polycrystalline forsterite

Rémi Delon, Sylvie Demouchy, Yves Marrocchi, Mohamed Ali M.A. Bouhifd, Julien Gasc, Patrick Cordier, Sanae Koizumi, Pete G Burnard

### ► To cite this version:

Rémi Delon, Sylvie Demouchy, Yves Marrocchi, Mohamed Ali M.A. Bouhifd, Julien Gasc, et al.. Effect of deformation on helium storage and diffusion in polycrystalline forsterite. *Geochimica et Cosmochimica Acta*, 2020, 273, pp.226-243. 10.1016/j.gca.2020.01.018 . hal-02951459

**HAL Id: hal-02951459**

**<https://hal.science/hal-02951459>**

Submitted on 30 Sep 2020

**HAL** is a multi-disciplinary open access archive for the deposit and dissemination of scientific research documents, whether they are published or not. The documents may come from teaching and research institutions in France or abroad, or from public or private research centers.

L'archive ouverte pluridisciplinaire **HAL**, est destinée au dépôt et à la diffusion de documents scientifiques de niveau recherche, publiés ou non, émanant des établissements d'enseignement et de recherche français ou étrangers, des laboratoires publics ou privés.

# Effect of deformation on helium storage and diffusion in polycrystalline forsterite

Rémi Delon<sup>1,\*</sup>, Sylvie Demouchy<sup>2</sup>, Yves Marrocchi<sup>1</sup>, Mohamed Ali Bouhifd<sup>3</sup>, Julien Gasc<sup>1,2</sup>,  
Patrick Cordier<sup>4</sup>, Sanae Koizumi<sup>5</sup> and Pete G. Burnard<sup>1</sup>

<sup>1</sup>Centre de recherches pétrographiques et géochimiques, UMR 7358, Université de Lorraine & CNRS, 15 rue  
Notre Dame des Pauvres, 54500 Vandoeuvre-lès-Nancy, France.

<sup>2</sup>Géosciences Montpellier, UMR 5243, Université de Montpellier & CNRS, Montpellier, France.

<sup>3</sup>Laboratoire Magmas et Volcans, UMR 6524, Université Clermont Auvergne & CNRS, Aubière, France.

<sup>4</sup>Univ. Lille, CNRS, INRA, ENSCL, UMR 8207 - UMET - Unité Matériaux et Transformations, F-59000 Lille,  
France

<sup>5</sup>Earthquake Research Institute, University of Tokyo, Tokyo, Japan

\* Corresponding author: remi.delon@uca.fr. Now at « Laboratoire Magmas et Volcans, UMR 6524, Université  
Clermont Auvergne & CNRS, 6 avenue Blaise Pascal, Aubière, France ».

Submitted to *Geochimica et Cosmochimica Acta* in May 2019

Revised for *Geochimica et Cosmochimica Acta* in January 2020

Accepted 11 january 2020, online 21 January 2020

## Abstract

Although recent studies have investigated He behavior in undeformed mantle minerals, the effect of defects generated by plastic deformation on He storage and transport remains unconstrained. For this purpose, synthetic dense aggregates of fine-grained iron-free forsterite were deformed under 300 MPa confining pressure at 950, 1050, and 1200 °C using a Paterson press. Three deformed samples and one undeformed sample were then doped with He under static high-pressure ( $1.00 \pm 0.02$  GPa) and high-temperature ( $1120 \pm 20$  °C) conditions for 24 h in a piston cylinder. Uraninite was used as a source of noble gases. The samples were subsequently analyzed using a cycled step heating protocol coupled with noble gas mass spectrometry to investigate He storage and diffusion in the deformed polycrystalline forsterite aggregates. Results show complex diffusive behaviors that cannot be fitted by a single linear regression. Nevertheless, individual step heating cycles can be fitted by several linear regressions determined by a *F*-test, suggesting that diffusivities follow Arrhenius law within the given temperature ranges. Our results highlight the complex diffusive behavior of He in deformed forsterite aggregates, which is due to the competition between several diffusion mechanisms related to different He storage sites (Mg vacancies, interstitial sites, dislocations, and grain boundaries). Diffusion parameters (activation energy  $E_a$  and pre-exponential factor  $D_0$ ) for He diffusion in grain boundaries were refined from literature data ( $E_a = 36 \pm 9$  kJ·mol<sup>-1</sup> and  $D_0 = 10^{-10.57 \pm 0.58}$  m<sup>2</sup>·s<sup>-1</sup>), and those of He diffusion in interstitials ( $E_a = 89 \pm 7$  kJ·mol<sup>-1</sup> and  $D_0 = 10^{-8.95 \pm 1.16}$  m<sup>2</sup>·s<sup>-1</sup>) and Mg vacancies ( $E_a = 173 \pm 14$  kJ·mol<sup>-1</sup> and  $D_0 = 10^{-5.07 \pm 1.25}$  m<sup>2</sup>·s<sup>-1</sup>) were defined from our results and literature data. Furthermore, we determined  $E_a = 56 \pm 1$  kJ·mol<sup>-1</sup> and  $D_0 = 10^{-9.97 \pm 0.37}$  m<sup>2</sup>·s<sup>-1</sup> for He diffusion along dislocations. These results suggest that a maximum He fraction of only 1.2% can be stored along dislocations in mantle minerals, which is negligible compared to 22% in grain boundaries as reported by previous studies. This implies that bulk lattice diffusivities are barely affected by the presence of

dislocations, whereas the proportion of He stored in grain boundaries can significantly enhance the bulk diffusivities of mantle rocks. Thus, deformation processes can significantly increase He storage capacity by decreasing grain size (i.e., via dynamic recrystallization), but will not sufficiently increase the dislocation density to induce a change in He storage and mobility within the crystallographic lattice. Furthermore, rapid redistribution of He between the mineral lattice and grain boundaries could enhance the bulk He concentrations of deformed peridotites upon equilibration with nearby undeformed (or less-deformed) peridotites.

*Keywords:* helium, diffusion, storage, deformation, dislocation, forsterite

## *1. Introduction*

The behavior of noble gases in the Earth's mantle provides important information and essential time constraints on chemical and isotopic mantle heterogeneities. Indeed, noble gases have both primordial and radiogenic isotopes and behave as both incompatible and volatile elements. Although they are not expected to be easily recycled during subduction processes (Moreira and Raquin, 2007; Staudacher and Allègre, 1988), several studies have reported evidences for noble gas recycling in the mantle (e.g., Holland and Ballentine, 2006; Parai and Mukhopadhyay, 2015; Kendrick et al., 2018; Smye et al., 2017). Nevertheless, differences in noble gas concentrations and isotopic ratios are still observed between mid-oceanic ridge basalts (MORBs) and ocean island basalts (OIBs), reflecting their different mantle sources (see Moreira, 2013, for a review). Helium (He) is a reliable tracer of mantle heterogeneities since its concentration is higher in MORBs than in OIBs (e.g., Moreira and Kurz, 2013), and the  $^3\text{He}/^4\text{He}$  ratio ( $R$ ) normalized to the atmospheric  $^3\text{He}/^4\text{He}$  ratio ( $R_a$ ) is homogeneous in MORBs (i.e.,  $R/R_a = 7-9$ ; e.g., Barfod et al., 1999), but varies from 4 (e.g.,

Farley et al., 1991; Moreira et al., 1999) up to almost 50 in OIBs (e.g., Hilton et al., 1997; Hiyagon et al., 1992; Honda et al., 1993; Kaneoka et al., 1983; Kurz et al., 1982, 1983; Rison and Craig, 1983; Starkey et al., 2009; Stuart et al., 2003; Valbracht et al., 1997). This dichotomy between MORBs and OIBs highlights the presence of at least two different sources in the Earth's mantle: (i) a primitive, less degassed source with low  $U/^3He$  and high  $R/Ra$  ratios as the source of OIBs, and (ii) a more degassed source with higher  $U/^3He$  as the source of MORBs (e.g., Moreira and Kurz, 2013).

Although macroscopic models have been developed to explain the existence of these reservoirs by isolating the OIB source from mantle convection (Allègre, 1987; Bouhifd et al., 2013; Coltice et al., 2011; Labrosse et al., 2007; Porcelli and Halliday, 2001), the fundamental physical behavior of He in mantle minerals (e.g., storage sites, diffusion mechanisms) remained poorly understood despite recent improvements. Helium can be stored in various atomic defects within the crystal structure, such as 0-dimension defects (i.e., Mg vacancies and interstitial sites in olivine; Delon et al., 2018), 1-dimension defects (dislocations), 2-dimensions defects (i.e., interfaces and grain boundaries; Baxter et al., 2007; Burnard et al., 2015; Delon et al., 2018), and 3-dimensions defects (i.e., inclusions; Trull and Kurz, 1993). The storage of He in multiple sites induces a complex diffusive behavior due to the competition between different diffusion mechanisms related to each storage site. This complex diffusive behavior is shown schematically in Figure 1 by considering site-specific diffusion rates depending on the relative degree of disorder of the crystalline structure in each site (i.e., faster diffusion in more disordered sites). Regarding 1-dimension defects, Piazzolo et al. (2016) showed using atom probe tomography that incompatible elements are preferentially stored along dislocations in zircon. Nevertheless, their transport along dislocations remains poorly constrained.

Ar storage and transport in deformed minerals has been investigated in thermochronological studies, which showed that bulk diffusivities increase with deformation, thus decreasing Ar retention and producing younger Ar-Ar ages (Dunlap and Kronenberg, 2001; Heizler et al., 1997; Kramar et al., 2001; Mulch et al., 2002; Reddy et al., 1996, 1999, 2001). Recent studies have reported abnormally high concentrations of Ar near crystal surfaces for several minerals including quartz and feldspar (Baxter et al., 2006; Clay et al., 2010; Kelley et al., 2008; Watson and Cherniak, 2003), olivine and pyroxene (Thomas et al., 2008; Watson et al., 2007), and plagioclase (Wartho et al., 2014). These high Ar concentrations imply very low diffusivities that have been interpreted as representative of Ar lattice diffusivities, although recent bulk degassing experiments suggest a surface effect (e.g., Burnard et al., 2015; Cassata et al., 2011; Delon et al., 2019). Such surface effects in mechanically prepared samples are in agreement with the study of Pinilla et al. (2012), who showed that diffusivities observed in the near-surface are not representative of bulk diffusivities due to the effect of interface adsorption, trapping Ar in dislocations, voids, and channels.

Although these results confirm the storage of noble gases in 1-dimension defects, abnormally high surface concentrations of He have only been observed in apatite (Van Soest et al., 2011), and the behavior of He in deformed minerals remains unconstrained. In this study, synthetic fine-grained polycrystalline iron-free forsterite was deformed at different temperatures, then experimentally doped with He at high pressure and high temperature. We analyzed the samples by step heating experiments to investigate He storage sites and diffusion in mantle olivine.

## 2. Materials and methods

### 2.1. Starting materials and deformation experiments

Forsterite samples used in this study were synthesized at the Earthquake Research Institute (Tokyo, Japan) from synthetic nano-powder made from colloidal SiO<sub>2</sub> (30 nm grain size) and Mg(OH)<sub>2</sub> (50 nm grain size). The sintering procedure was previously described by Koizumi et al. (2010) and is briefly summarized here. The powders were dispersed and mixed by ball milling for one day at a rate of ~250 rpm using 10-mm nylon-covered balls with iron cores and high-purity ethanol as a solvent. The samples were then dried at ~60 °C while stirring. The resulting powder was calcinated using an alumina tube furnace at 960 °C for 3 hours under an oxygen flow to remove decomposed products (H<sub>2</sub>O and CO<sub>2</sub>). The samples were pulverized with an agate mortar and pelletized using tungsten carbide dies to obtain disc-shaped samples, which were wrapped in a rubber sleeve and evacuated with a rotary pump. The compacted samples were then dropped into a water-medium pressure vessel and cold-pressed at 200 MPa for 10 min to produce pellets. The pellets were placed on a platinum crucible or plate in an alumina tube furnace with a vacuum diffusion pump and sintered at 1260 °C for 2–3 h. The sintering conditions were carefully selected to maximize densification and minimize grain growth. The final porosity of the pellets was well below 1 vol.% (for further details, see Koizumi et al., 2010). The final products contained a low proportion (<2%) of iron-free enstatite to buffer the silica activity, but this abundance is too low to significantly modify the bulk diffusivities obtained during the subsequent step heating experiments (see section 4.1).

After sintering, the four cylindrical samples (NF\_SM, NF\_1200-1, NF\_1050-1, and NF\_950-1) had diameters of 4.5–4.8 mm and lengths of 7.25–10.55 mm. Three of them (NF\_1200-1, NF\_1050-1, and NF\_950-1) were used in deformation experiments performed at Geosciences Montpellier (University of Montpellier, France) in a gas-medium high pressure-high temperature apparatus (Paterson press; Paterson, 1990; Thieme et al., 2018). These samples were fit into metal sleeves (NF\_1200-1, NF\_1050-1, and NF\_950-1 into nickel,

copper, and silver sleeves, respectively), placed between alumina and zirconia pistons (Demouchy et al., 2014; Mei and Kohlstedt, 2000), and the assembly was encapsulated in an iron jacket. Deformation experiments were performed under uniaxial compression in an isostatic Ar pressure of 300 MPa at temperatures of 1200, 1050, and 950 °C for NF\_1200-1, NF\_1050-1, and NF\_950-1, respectively. Mechanical data and texture characterizations are fully reported in Gasc et al. (2019). After the deformation experiments, the samples were hand-polished to remove the metal sleeve and cut with a slow speed saw into millimeter-sized cubes. A first part of the recovered deformed fine-grained forsterite was used as starting material for doping experiments at high pressure and high temperature, and a second part was prepared for scanning electron microscopy (SEM), electron backscattered diffraction (EBSD) and transmission electron microscope (TEM) analyses for post-deformational grain size quantification and textural and microstructural characterization.

SEM and EBSD analyses were performed at Geosciences Montpellier with a CamScan X500FE Crystal Probe (see Demouchy et al., 2012) equipped with an EBSD system. Sample sections were prepared using a standardized polishing protocol (e.g., Thieme et al., 2018) and a final polishing step was performed using colloidal silica on a vibrating plate to obtain a high-quality polish for EBSD observation. Operating conditions were 15–18 kV and 6 or 10 nA (for exposure times of 48 and 24 ms, respectively) at a working distance of 24–25 mm under low vacuum conditions (5 Pa of gaseous nitrogen) to avoid charging on the sample. Samples were carbon-coated and surrounded by copper-carbon conductive tape for EBSD analyses. EBSD maps were acquired with a step size of 0.2 or 0.4  $\mu\text{m}$ , allowing the grain size distributions to be determined after data treatment (Demouchy et al., 2014; Gasc et al., 2019).

For TEM analyses, post-deformation pre-doped samples were doubly polished to obtain 30- $\mu\text{m}$ -thick thin sections, and glued on a Cu grid before ion milling at 5 kV under a low beam angle of 15° to reach electron transparency. The resulting foils were carbon-coated and



observed in a FEI® Tecnai G2-20 twin microscope operating at 200 kV at Unité Matériaux et Transformations (University of Lille, France).

## *2.2. Doping experiments*

The deformed (NF\_1200-1, NF\_1050-1, and NF\_950-1) and undeformed (NF\_SM) samples were doped at high pressure and high temperature in the presence of a  $^4\text{He}$  source following a similar protocol described in Burnard et al. (2015), which was developed to mimic sub-solidus mantle conditions at low to medium noble gas partial pressure. In this study, the  $^4\text{He}$  source was uraninite powder from Mistamisk, Canada (for details, see Kish and Cuney, 1981). Doping experiments were performed at the Laboratoire Magmas et Volcans (Université Clermont Auvergne, Aubière, France) in a 3/4" piston cylinder. The samples were hand-polished to fit in 9-mm-long Pt capsules with an outer diameter of 5 mm and an inner diameter of 4.5 mm. Each sample was placed in a Pt capsule and separated from the uraninite powder by two Pt discs to avoid contamination of the samples by the He source, and any empty space was filled with San Carlos olivine powder, as shown in Fig. 2. The capsule was then closed by welding two Pt lids at each end, loaded in a Pyrex cylinder with two MgO cylinders at each end, and surrounded by MgO powder. The assembly was slid into a graphite furnace and placed in a Pyrex cylinder and a NaCl sleeve to ensure efficient pressure transmission and inhibit the occurrence of water (Fig. 2). Temperature was controlled and monitored using a  $\text{W}_5\text{Re}/\text{W}_{26}\text{Re}$  thermocouple (C-type) at the base of the Pt capsule (Fig. 2). External calibrations show a temperature gradient of less than 20 °C along the Pt capsule. The samples were annealed at  $1120 \pm 20$  °C and  $1.00 \pm 0.02$  GPa for ~24 h, and were quenched at high pressure. This long annealing stage at  $T > 1100$  °C and 1 GPa ensures complete collapse of residual porosity (from hot press at 300 MPa), closing up potential open grain boundaries (from grain sliding, see Gasc et al., 2019) and providing further dense sintering. At 1100 °C

and after 24 h only, intracrystalline ductility features are expected to be preserved (Farla et, 2011). After the doping experiments, the samples were extracted from the capsules and cut into millimeter-sized cubes. For each sample, a single cube from the core was carefully selected to ensure that residual uraninite was not present during the subsequent noble gas analyses. Experimental conditions are summarized in Table 1.

### 2.3. Helium analyses

Helium analyses were performed using a cycled step heating protocol coupled with noble gas mass spectrometry, as detailed in Delon et al. (2018). Samples were annealed at different temperature steps and the gas extracted during each heating step was analyzed to obtain the molar quantity of He released, which permits calculation of the fractional gas loss and thus of the diffusion coefficient ( $D$ ) as a function of the square of the radius of the diffusion domain ( $a$ ). The corresponding equations were modified from Crank (1975), Fechtig and Kalbitzer (1966), and McDougall and Harrison (1999), and are presented in detail in Delon et al. (2018). Since  $D$  is related to temperature ( $T$ ) by an Arrhenius equation,  $D = f(1/T)$  (or  $D/a^2$  if  $a$  is unknown) permits to obtain (i) the activation energy ( $E_a$ ), and (ii) the pre-exponential factor ( $D_0$  or  $D_0/a^2$  if  $a$  is unknown). Although the equations used to determine  $D$  were developed considering a homogeneous initial concentration in the sample, Delon et al. (2018) have already redeveloped them for heterogeneous initial concentration profiles. They reported no major change in the resulting diffusion parameters (within the error bars). Thus, even if samples were only partially doped, it does not impact the diffusion parameters calculated in this study.

Step heating analyses were performed at the Centre de Recherches Pétrographiques et Géochimiques (CNRS, Université de Lorraine, Nancy, France) using a Helix MC mass spectrometer, which was calibrated using aliquots ( $\sim 0.3$  cc,  $\sim 1.57 \times 10^{-8}$  mol) of an in-house

200 He standard (for further details, see Matsuda et al., 2002). The  $^4\text{He}$  signal was collected on a  
201 Faraday cup coupled with a  $10^{11} \Omega$  amplifier. A standard analysis was performed between  
202 each sample analysis, and the analytical sensitivity was calculated and used to obtain the  
203 molar quantity of He extracted during each heating step. The external error determined from  
204 these sensitivities was less than 8%, which represents a maximum external error of  $\pm 0.04$  on  
205 the resulting  $\log(D/a^2)$  values. Samples were loaded into a filament furnace, which consists of  
206 four alumina-coated tungsten evaporation baskets welded to two nickel rods as described in  
207 Bekaert et al. (2018). The furnace was calibrated by the melting points of tin, aluminum,  
208 copper and nickel, and the calibration curve (temperature as a function of the current) was  
209 obtained by second-order polynomial regression on the melting points. Before sample  
210 loading, the filament was degassed at  $\sim 1600^\circ\text{C}$  under high vacuum for 1 h to remove any  
211 adsorbed atmospheric gases. A blank analysis was performed at  $\sim 1400^\circ\text{C}$  before sample  
212 introduction (releasing  $8.69 \times 10^{-15}$  mol of He), and a cold blank analysis was performed for  
213 each sample: the molar quantities extracted during cold blank analyses represented less than  
214 10% ( $\sim 2.90 \times 10^{-15}$  mol) of those extracted during each heating step. Because of high blank  
215 signals, sample NF\_1200-1 was degassed under vacuum for 1 h at  $800^\circ\text{C}$  before the step  
216 heating experiments to remove any gas adsorbed onto the sample surface, which greatly  
217 improved the blank signals. During this degassing step, He was lost and not analyzed, which  
218 can modify the initial He concentration profile of the sample. Nevertheless, a change in the  
219 initial concentration profile does not modify the resulting diffusion parameters (Delon et al.,  
220 2018). At each heating step, the temperature was held for 30 min, and the extracted gas was  
221 purified and analyzed, background and blank corrections were performed. Step heating  
222 experiments were cycled, meaning that each sample underwent several step heating sequences  
223 (cycles). A cycle consists in increasing the temperature between two heating steps, whereas  
224 the temperature is decreased at the end of a cycle to perform a second cycle on the same

sample, and so on. This protocol is used in thermochronology to identify diffusion domains that are not replenished (e.g., Reiners and Farley, 1999; Reiners et al., 2004) and has proved efficient for characterizing He storage sites in polycrystalline olivine (Delon et al., 2018). Individual step sequences are presented in Table 1. At the end of the cycled step heating experiments, the samples were fused at above 2000 °C and the extracted gas was analyzed to determine the total amount of He stored in the corresponding sample, and to back-calculate the fractional gas loss during each temperature step.

### 3. Results

#### 3.1. Textures and microstructures

Representative SEM and TEM images of pre-doped samples are displayed in Fig. 3, and additional images are available in Gasc et al. (2019). The average grain sizes determined from EBSD maps are reported in Table 1 and only slightly decreased during the deformation experiments. Grain size variations are expected to be negligible during the doping experiments since the diffusion length of silicon is only 0.56 nm in dry olivine (Dohmen et al., 2002) and 47 nm in wet olivine (Costa and Chakraborty, 2008) at the conditions of the doping experiments (i.e., 1120 °C and 24 h). SEM images of the four pre-doped samples show granoblastic textures with equilibrated triple junctions (Fig. 3a–d). Grain boundaries are mostly straight in samples NF\_SM, NF\_950-1, and NF\_1050-1, whereas they are occasionally slightly curved in NF\_1200-1. All samples have low porosities. Porosity appears to be more important in samples deformed at low temperature because they show grain boundaries opened by sliding, which creates voids during the deformation experiments (Gasc et al., 2019). If preserved during annealing at 1 GPa, these 3-dimensions defects can trap noble gases during doping experiments, and their release can significantly impact the calculated diffusivities obtained during the step heating experiments. However, no gaps and voids are

expected to subsist under 1 GPa (e.g., German, 2014). Furthermore, several grains in the deformed samples showed internal contrast variations, highlighting the formation of subgrain boundaries (i.e., walls of dislocations), demonstrating that intracrystalline ductile deformation occurred (Fig. 3b–d).

TEM images show microstructures typical of deformed samples (i.e., straight dislocations, few dislocation loops, sub grain boundaries, Fig. 3e–h). These microstructures are mainly heterogeneous and due to microplasticity. Rare nanobubbles were also observed, which could act as a trap for He during doping experiments. In summary, the deformation experiments successfully involve 1-, 2-, and 3-dimensions defects (i.e., dislocations, subgrains, grain boundaries, and nanobubbles, respectively). We calculated the dislocation density ( $\rho$  in  $\text{m}^{-2}$ , i.e., total length of dislocations in a unit volume of a crystal) for each deformed sample using Ham's (1961) method, which consists in drawing straight lines of cumulative length  $L$  in random directions on a TEM image and counting the number of dislocations ( $N$ ) intersecting these lines. Using the sample thickness  $e$  (i.e., ~200 nm), dislocation density is estimated as:

$$\rho = \frac{2N}{L \cdot e} \quad . \quad (1)$$

We applied this method for four TEM images for sample NF\_950-1, one for NF\_1050-1, and three for NF\_1200-1, which were selected as being characteristic of the samples. The results confirm high dislocation densities for each deformed sample with mean values of  $2.3 \pm 1.2 \times 10^{13} \text{ m}^{-2}$  for NF\_950-1,  $8.1 \times 10^{13} \text{ m}^{-2}$  for NF\_1050-1, and  $5.8 \pm 1.5 \times 10^{13} \text{ m}^{-2}$  for NF\_1200-1.

### 3.2. Helium diffusivity

Helium diffusivities are reported in Fig. 4 and the detailed data treatment is provided in supplementary file. The results show diffusive behavior that does not follow a single Arrhenius law since abrupt changes in slope occur in each Arrhenius diagram. Thus, our data

cannot be fitted with only one linear regression, suggesting different diffusion mechanisms at different temperature ranges. The best fit of our data by one, two, or three linear regressions and the associated transition temperatures were determined using  $F$ -tests on each cycle. Further details and results of the  $F$ -tests are available in supplementary material. The  $F$ -test is used to compare two models, and if the resulting  $F$  value is greater than the critical  $F$  value (available in  $F$  tables), the model with the fewest parameters is rejected. Otherwise, we chose the simpler model with the fewest parameters to fit our data (e.g., Box, 1953; Chow, 1960; Hahs-Vaughn and Lomax, 2013). For each cycle, we performed a  $F$ -test between a single linear regression (model 1) and all possible fits with two linear regressions (model 2, excluding all linear regressions fitted with less than three data points as irrelevant). If model 1 was rejected, we compared the best-fit model with two linear regressions to models with three linear regressions, and so on. In the case where several models resulted in rejecting the comparative model, we chose the model with the greatest  $F$  value as the comparative model in subsequent tests or as the best fit to our data.

The linear regressions resulting from the  $F$ -tests are plotted in Fig. 4. The resulting diffusion parameters ( $E_a$  and  $D_0$  as a function of  $a^2$ ) are reported in Table 2 and vary widely:  $E_a$  varied from  $3 \pm 6$  to  $330 \pm 29$  kJ·mol<sup>-1</sup> and  $\log(D_0/a^2)$  ( $D_0$  in m<sup>2</sup>·s<sup>-1</sup> and  $a$  in m) from  $-9.44 \pm 0.82$  to  $7.98 \pm 1.29$ . This variation suggests a complex behavior of He diffusion in polycrystalline forsterite, with competition between different diffusive processes. However, since models with several linear regressions can fit our data, we can reasonably assume that diffusivities follow Arrhenius equations over the temperature ranges determined from the  $F$ -tests. These results were obtained by excluding some data points (open symbols in Fig. 4) at very low temperature (one each for NF\_SM and NF\_950-1) and at very high temperature (one for NF\_950-1 and two for NF\_1050-1) because they were considered as being distinctly different from the trend described by the nearby points.

299

## 300 4. Discussion

### 301 4.1. Mechanisms of He diffusion

302 The results of the  $F$ -tests show that models with several linear regressions for each cycle  
303 are the most relevant to fit our data. Thus, He diffusivity in our samples is complex, arising  
304 via competition between different diffusion mechanisms. Several hypotheses may explain  
305 why the diffusivities do not follow a single Arrhenius law: (i) the presence of a multi-  
306 diffusion domain (e.g., Harrison and Lovera, 2014; Lovera, 1992; Lovera et al., 1989), (ii) a  
307 competition between intrinsic and extrinsic diffusion at the atomic scale (e.g., Chakraborty,  
308 1997, 2008; Dohmen, 2008; Dohmen and Chakraborty, 2007), or (iii) a contribution of  
309 different diffusion mechanisms related to different storage sites, as has been observed for  
310 hydrogen (Demouchy, 2010; Mackwell and Kohlstedt, 1990; Padrón-Navarta et al., 2014;  
311 Thoraval and Demouchy, 2014), He, and Ar diffusion in undeformed polycrystalline olivine  
312 (Burnard et al., 2015; Delon et al., 2018, 2019). Because  $E_a$  values vary among linear  
313 regressions and transition temperatures differ between samples and even cycles, we favor the  
314 third hypothesis (see also Delon et al., 2018).

315 To confirm this hypothesis, we compare the diffusion parameters calculated from this  
316 study ( $E_a$  and  $\log D_0$ ) to those obtained for the different diffusive mechanisms observed in  
317 Burnard et al. (2015) and Delon et al. (2018) in Fig. 5. To calculate  $\log D_0$ ,  $a$  was chosen as  
318 half the sample size during the step heating experiments (i.e., 1 mm in this study), as was  
319 previously demonstrated in Delon et al. (2018). We follow the same usage as Delon et al.  
320 (2018) with LAT-high referring to diffusion in Mg vacancies, LAT-low to diffusion in  
321 interstitial sites, LAT to diffusion in the crystal lattice (i.e.,  $\text{LAT} = \text{LAT-high} + \text{LAT-low}$ ),  
322 and GB to grain boundary diffusion; when bulk diffusion is controlled by diffusion in several  
323 storage sites (co-governance), the implicated diffusions are separated by the + sign. The

formalisms of these different diffusive mechanisms are displayed in Table 3. The above studies showed that He diffusion in polycrystalline olivine occurs via LAT-high, LAT-high + LAT-low, and LAT + GB mechanisms, and we show the mean values (and the standard deviations) over which those mechanisms were reported to occur in Fig. 5. Most of the  $E_a$  and  $\log D_0$  values from this study plot within those ranges, suggesting that LAT-high, LAT-high + LAT-low, and LAT + GB mechanisms were also observed in our diffusion experiments. Thus, the apparent non-Arrhenian behavior is due to diffusion mechanisms related to different storage sites, and transitions occurred upon the depletion of He in a storage site.

However, some diffusion parameters obtained herein clearly differ from those of the LAT-high, LAT-high + LAT-low, and LAT + GB mechanisms. Some  $E_a$  values are below the LAT + GB range (i.e.,  $<11 \text{ kJ}\cdot\text{mol}^{-1}$ ); these values seem to agree with those reported by Burnard et al. (2015) for Ar surface diffusion in olivine. Although the species are different, comparison between He and Ar surface diffusion is relevant in terms of  $E_a$ , but not in terms of  $D_0$ . Indeed, the  $E_a$  for He surface diffusion is expected to be lower than that for LAT + GB mechanisms since He is only retained by Van der Waals bonds (i.e., low-energy interactions) at the sample surface. Furthermore, a low  $E_a$  value and one consistent with LAT + GB diffusion were obtained at lower and higher temperatures, respectively, during the same cycle (NF\_1050-1, cycle 1, Figs. 4 and 5), demonstrating that this low  $E_a$  mechanism (surface diffusion) is distinct from the LAT + GB mechanisms, and not simply LAT + GB diffusion with an abnormally low  $E_a$ .

Two  $E_a$  values (NF\_SM, cycle 1, and NF\_950-1, cycle 2) are near the lower limit of the LAT-high range. Instead of interpreting these as the LAT-high mechanism, we rather propose that the corresponding linear regressions were influenced by both the LAT-high and the LAT-high + LAT-low mechanisms. Indeed, Delon et al. (2018) demonstrated that a single regression encompassing these two mechanisms induced  $E_a$  and  $\log D_0$  values between those



for the LAT-high and LAT-high + LAT-low mechanisms (as in Blard et al., 2008; Cherniak and Watson, 2012), whereas performing two linear regressions on the same data points (one at lower temperature and another at higher temperature) returns values in agreement with those of the separate LAT-high and LAT-high + LAT-low mechanisms. We tested this by reprocessing these data points using three linear regressions instead of two (detailed results are reported in Table 2). Although the two-linear regression models presented for these samples in Fig. 4 were not rejected by the *F*-tests, the models with three linear regressions seem more suitable since the reprocessed data show diffusion parameters consistent with the distinct ranges of LAT-high and LAT-high + LAT-low mechanisms.

Diffusion parameters calculated from cycle 4 of sample NF\_SM do not seem to correlate with data from previous studies. This cycle was characterized by an abrupt increase of He release, inducing first a high  $E_a$  ( $\sim 330 \text{ kJ}\cdot\text{mol}^{-1}$ ) then a moderate  $E_a$  ( $\sim 120 \text{ kJ}\cdot\text{mol}^{-1}$ ). A similar burst in noble gas release was observed for Ar in pyroxenes and occurs upon early partial melting of the sample (Cassata et al., 2011). However, early partial melting of olivine has never been reported below 1100 °C (under a pressure of 1-atm, Jaoul et al., 1987). Alternatively, He trapped in 3-dimensions defects (i.e., pores, voids) could significantly increase the release of He (and thus the resulting diffusivities), especially at high temperature. Indeed, the high  $E_a$  reported by Trull and Kurz (1993) for He diffusion in olivine has been interpreted as an energy of remobilization of He trapped in melt inclusions (e.g., Blard et al., 2008; Cherniak and Watson, 2012; Tolstikhin et al., 2010), highlighting the high-temperature dependency of this release. Thus, a minor contribution of He trapped in pores can significantly increase the apparent He release at high temperature and thus the resulting diffusivities, as observed in the diffusivities obtained for cycle 4 of sample NF\_SM (Fig. 4). A similar event could also explain the abnormal  $E_a$  values obtained for sample NF\_1200-1; two values are well above the LAT-high range, and another obtained at the highest

temperature range is abnormally low and thus does not actually correspond to LAT-high +  
 LAT-low mechanisms. Another possibility to explain these abnormal diffusion parameters is  
 the presence of enstatite in our samples. Indeed, orthopyroxene is more Ar-retentive than  
 olivine since Ar diffusivities in orthopyroxene are significantly smaller than those in olivine  
 (e.g., for orthopyroxene, see Cassata et al., 2011; for olivine, see Futagami et al., 1993; Delon  
 et al., 2019), and this difference decreases with increasing temperature: for Ar, at 400 °C,  
 $\log D \sim -19.92$  in olivine and  $-30.03$  in orthopyroxene, whereas at 1200 °C,  $\log D \sim -12.93$   
 and  $-14.40$  in olivine and orthopyroxene, respectively, with  $D$  in  $\text{m}^2 \cdot \text{s}^{-1}$ ). We note that similar  
 diffusive behavior is expected for He in olivine and orthopyroxene, and thus a relatively small  
 He release from enstatite is predicted at low temperature whereas enstatite can significantly  
 contribute to the He release at high temperature, resulting in enhanced calculated diffusivities,  
 as shown in Fig. 4. A final explanation to interpret these high activation energies could be the  
 absence of iron in our samples compared to those in Delon et al. (2018). Indeed, the  
 incorporation of iron was proposed to impact the strength of olivine and the incorporation of  
 hydrogen in olivine at pressure below 1 GPa (Zhao et al., 2001, 2009). The substitution of Mg  
 by  $\text{Fe}^{3+}$  should create additional vacancies and enhance transport properties such as ionic  
 diffusion (Nakamura & Schmalzried, 1984). Thus, it should decrease the activation energy.  
 Although some activation energies are higher in this study than in Delon et al. (2018) for  
 diffusion in Mg-vacancies, this is not systematically true, suggesting that an increase in  
 activation energy is not due to the absence of iron the crystal lattice. An explanation for the  
 consistent absence of iron effect could be that the number of defects created by the  
 substitution of magnesium by iron is too low to significantly modify the mean distance  
 between two Mg-vacancies and thus, the activation energy.

A last set of diffusion parameters observed only in deformed samples (NF\_950-1,  
 NF\_1050-1, and NF\_1200-1) remains unexplained. The values of these diffusion parameters

are similar among the three samples, with mean values of  $E_a = 56 \pm 1 \text{ kJ}\cdot\text{mol}^{-1}$  and  $\log D_0 = -9.97 \pm 0.37$  ( $D_0$  in  $\text{m}^2\cdot\text{s}^{-1}$ ). Although the pre-exponential factors are in the LAT-high + LAT-low range, the  $E_a$  values plot between the LAT-high + LAT-low and LAT + GB ranges. As these diffusion parameters occurred only in deformed samples, they are interpreted as corresponding to the combined contribution of lattice diffusion and diffusion along dislocations (LAT + DIS). Indeed, the  $E_a$  values suggest that the corresponding storage site is less retentive than the crystal lattice but more than grain boundaries, and are thus associated with dislocations that occur in deformed samples. To investigate the He amount stored along dislocations in our samples, the approximation that He extracted during heating steps, which expressed the LAT + DIS mechanisms, can be done. It yields that  $5.79 \times 10^{-13}$ ,  $1.86 \times 10^{-11}$ , and  $1.99 \times 10^{-12}$  mol of He are stored along dislocations for NF\_950-1, NF\_1050-1, and NF\_1200-1, respectively. Nevertheless, since each sample was doped separately with different starting amount of He, it is difficult to determine if these amounts represent solely a difference in dislocation density or results also from the experimental run conditions. For these reasons, He storage as a function of the absolute density in dislocations in our samples will not be discussed any further.

#### 4.2. Diffusion along dislocations

Here, we extract the diffusivities along dislocations from the bulk diffusivities expressed in the LAT + DIS temperature range for deformed samples. Similar to grain boundary diffusion, bulk diffusivities resulting from the combined contribution of lattice diffusion and diffusion along dislocations can express three kinetic regimes (e.g., Harrison, 1961; Lee, 1995): the A-regime is mainly controlled by diffusion in the crystal lattice, the C-regime is controlled only by diffusion along dislocations, and the B-regime is the intermediate case (for further details on these kinetic regimes applied to grain boundary diffusion, see Dohmen and

Milke, 2010; Joesten, 1991; Mishin and Herzig, 1995, 1999). These kinetic regimes evolve with diffusion time from the type C to the type B and ultimately to the type A regime. Thus, it is important to constrain which kinetic regime occurred in our diffusion experiments to identify the diffusion mechanism controlling the bulk diffusivities. The A-regime occurs for diffusion times ( $t$ ) significantly higher than the boundary time ( $t_d$ ), defined as:

$$t_d = \frac{l_d^2}{4D^{\text{LAT}}} \quad , \quad (2)$$

where  $l_d$  is the mean spacing between dislocations ( $l_d = \sqrt{1/\rho}$ ) and  $D^{\text{LAT}}$  the lattice diffusion coefficient. In our samples,  $l_d = 209$ ,  $111$ , and  $131$  nm in NF\_950-1, NF\_1050-1, and NF\_1200-1, respectively. At  $400$  °C (the lowest temperature step), these dislocation spacings yield  $t_d = 78$ ,  $22$ , and  $31$  s for NF\_950-1, NF\_1050-1, and NF\_1200-1, respectively, by considering the mean values of the lattice diffusion parameters obtained by Delon et al. (2018) and herein for the LAT-high + LAT-low mechanisms. Thus,  $t_d$  is significantly shorter than the extraction duration during a heating step ( $1800$  s), which means that the A-regime always occurred in the step heating experiments when the LAT + DIS mechanisms was expressed. In the A-regime, the bulk diffusion coefficient  $D^{\text{bulk}}$  can be calculated as a function of the diffusion coefficient along dislocations ( $D^{\text{DIS}}$ ) and the lattice diffusion coefficient as:

$$D^{\text{bulk}} = g \cdot D^{\text{DIS}} + (1 - g) \cdot D^{\text{LAT}} \quad , \quad (3)$$

where  $g$  is the fraction of the diffusing atoms that are located along dislocations. However, this equation was first derived by Hart (1957), but was developed assuming an equilibrium model in which the transfer of the diffusing species is in equilibrium at a local scale (Lee, 1995). Since our samples were partially doped, this assumption may not hold, and we will not extract  $D^{\text{DIS}}$  using Eq. (3).

Although theory predicts that the A-regime is expressed during the step heating experiments, the consistency of the  $E_a$  and  $\log(D_0)$  values expressed by the deformed samples in the LAT + DIS temperature range suggests that diffusion is mainly controlled by a single

447 mechanism here, diffusion along dislocations. To verify this hypothesis, we compared the  
 448 mean values of  $E_a$  and  $\log D_0$  expressed in the LAT + DIS temperature range with those of  
 449 diffusion along grain boundaries, in interstitial sites and in Mg vacancies (Fig. 6). Grain  
 450 boundary diffusion parameters are from Delon et al. (2018), obtained using the same method,  
 451 except that we performed a linear regression on four data points (instead of five) because the  
 452 lowest temperature diffusivity of their sample RDPC150 does not describe the same trend as  
 453 the other diffusivities expressing grain boundary diffusion: this reprocessing of the two data  
 454 sets (Delon et al., 2018 and this study) yields  $E_a = 36 \pm 9 \text{ kJ}\cdot\text{mol}^{-1}$  and  $\log D_0 = -10.57 \pm 0.58$ .  
 455 For diffusion in interstitial sites and in Mg vacancies, we use the mean values of the diffusion  
 456 parameters expressed in the LAT-high + LAT-low and LAT-high temperature ranges,  
 457 respectively, from Delon et al. (2018) and herein, leading to  $E_a = 89 \pm 7 \text{ kJ}\cdot\text{mol}^{-1}$  and  $\log D_0 =$   
 458  $-8.95 \pm 1.16$  for diffusion in interstitials and  $E_a = 173 \pm 14 \text{ kJ}\cdot\text{mol}^{-1}$  and  $\log D_0 = -5.07 \pm 1.25$   
 459 for diffusion in Mg vacancies. The diffusion equations corresponding to each diffusion  
 460 mechanism are displayed in Table 3. According to Fig. 6, the diffusivities expressed in the  
 461 LAT + DIS temperature range are bracketed between grain boundary and lattice diffusivities  
 462 for temperatures between 400 °C (i.e., below mantle temperatures) and 1400 °C (the highest-  
 463 temperature boundary of the olivine stability field; e.g., Akaogi et al., 1989). Only at high  
 464 temperature do Mg vacancy diffusivities exceed those of the other mechanisms. Thus, the  
 465 diffusivities obtained in the LAT + DIS temperature range are characteristic of a diffusion  
 466 mechanism in a storage site with a level of structure/disorder comprised between those of  
 467 point defects (i.e., interstitials, Mg vacancies) and 2-dimensions defects (i.e., grain  
 468 boundaries). Then, the logical possibility for this storage site is dislocations (1-dimension  
 469 defects) in the deformed samples. We thus interpret the diffusion coefficients obtained in the  
 470 LAT + DIS temperature ranges as representative of diffusion along dislocations with the  
 471 mean diffusion parameters  $E_a = 56 \pm 1 \text{ kJ}\cdot\text{mol}^{-1}$  and  $\log D_0 = -9.97 \pm 0.37$ . The enhancement

of He diffusion along dislocations is very modest as shown by Figure 6, except at very low temperature (below ca. 600 °C). Dislocations are often considered to be short circuit diffusion paths. Indeed, a recent measurement of impurity diffusivity along a single dislocation in aluminum has demonstrated a diffusivity enhancement of almost three orders of magnitude as compared with bulk diffusion (Legros et al. 2008). However, the situation varies strongly from a system to another since in SrTiO<sub>3</sub>, Marrocchelli et al. (2015) report no significant pipe diffusion of oxide ions at dislocation cores. In olivine, little data are available. Wolfenstine (1990) has interpreted low temperature creep data in single crystal of dry olivine based on the role of pipe diffusion. Gérard and Jaoul (1989) found no enhancement of oxygen diffusion by dislocations in San Carlos olivine, however, Yurimoto et al. (1992) reported diffusivities along dislocations for oxygen 10<sup>4</sup> times faster than lattice diffusivities in forsterite. To date, no diffusivity data are available for the role of dislocations on silicon diffusion, which is expected to be the creep rate limiting species. Our measurements represent the first indication of the role of dislocations on impurity diffusion in forsterite with a small effect on He diffusion, except at very low temperatures.

Nevertheless, at high temperature, diffusion in Mg vacancies shows higher diffusivities than the other diffusion mechanisms, contrary to what is expected. Diffusion in Mg vacancies might be more affected by increased pressure than the other diffusion mechanisms. Although no pressure effect has been observed up to 2.7 GPa for He lattice diffusion in olivine (Cherniak and Watson, 2012), first-principles calculations predict an influence up to 14 GPa (Wang et al., 2015), resulting in decreased diffusivity with increasing pressure. These results are in agreement with changes in Ni and Mn diffusivities in olivine with increasing pressure reported by Holzapfel et al. (2007). Since the compressibility of polyhedra increases with their size in the olivine lattice (e.g., Andraut et al., 1995), a similar assumption can be made for He storage sites in the olivine lattice. Thus, Mg sites should be more affected by

compression than interstitial sites, implying a greater decrease of He diffusivities via Mg vacancies with increasing pressure than via interstitials.

#### 4.3. Implications for the Earth's upper mantle

To assess the implications of He storage along dislocations within the olivine stability field (i.e., until 410 km depth; Akaogi et al., 1989; Katsura et al., 2004) and assuming that dislocation creep controls olivine plastic deformation in the entire upper mantle, we have calculated the amount of He stored in dislocations compared to that stored in the crystal lattice. This proportion ( $g$ ) can be defined as a function of the partition coefficient between dislocations and the lattice ( $K^{\text{dis/lat}}$ ) and the volume fraction of dislocations ( $v^{\text{DIS}}$ ) as demonstrated by Lee (1995):

$$g = \frac{K^{\text{dis/lat}} \cdot v^{\text{DIS}}}{(K^{\text{dis/lat}} - 1) \cdot v^{\text{DIS}} + 1} \quad (4)$$

Although  $K^{\text{dis/lat}}$  is not known, it must be greater than 1 since He is an incompatible element (e.g., Heber et al., 2007; Jackson et al., 2013) and less than  $10^5$  (the highest value of the He partition coefficient between a silicate melt and the olivine lattice, see Delon et al., 2018). Thus, to obtain the maximum fraction of He stored along dislocations, we chose the maximum value of  $10^5$  for  $K^{\text{dis/lat}}$ . The value of  $v^{\text{DIS}}$  can be determined from the dislocation density ( $\rho$ ), which is between  $10^{10}$  and  $10^{12} \text{ m}^{-2}$  in the deformed lithospheric mantle (e.g., Gueguen and Darot, 1980; Wallis et al., 2019), and the radius of the dislocation core ( $r$ ) as  $v^{\text{DIS}} = \rho \cdot \pi r^2$  (Lee, 1995). For lithospheric mantle conditions, the maximum fraction of He stored along dislocations can be calculated for  $\rho = 10^{12} \text{ m}^{-2}$ . This yields a maximum value of  $g$  of 1.2% for  $r = 2 \text{ \AA}$  (e.g., Durinck et al., 2007; Mahendran et al., 2017), meaning that only a negligible fraction of He (<1.2%) can be stored along dislocations in the Earth's upper mantle.

Concerning diffusion, the maximum value of  $t_d$  is obtained from Eq. (2) by considering a temperature of 900 °C (a realistic minimum lithospheric mantle temperature) and a low  $\rho$  value. However,  $\rho$  is only available in the literature for deformed peridotites with a minimum value of  $10^{10} \text{ m}^{-2}$  (e.g., Gueguen and Darot, 1980). Nevertheless, at 900 °C,  $t_d$  is greater than 1 yr for  $\rho < 10^6 \text{ m}^{-2}$  and  $t_d > 1 \text{ kyr}$  for  $\rho < 10^3 \text{ m}^{-2}$ . Thus, we can conclude that at geological time scales, the A-regime (which is expressed for durations greater than  $t_d$ ) always prevails in the Earth's mantle. Equation (3) can then be used to estimate bulk diffusivities in mantle minerals as a function of  $\rho$  and  $K^{\text{dis/lat}}$ . The influence of  $K^{\text{dis/lat}}$  is reported in Fig. 7 for a maximum value of  $\rho$  of  $10^{12} \text{ m}^{-2}$ , and the influence of  $\rho$  on bulk diffusivities is shown in the supplementary material for a reasonable  $K^{\text{dis/lat}}$  value of  $10^4$ . Bulk diffusivities increase with both  $K^{\text{dis/lat}}$  and  $\rho$ , but even at the maximum value of  $\rho$  observed in natural deformed peridotite (i.e.,  $10^{12} \text{ m}^{-2}$ ),  $K^{\text{dis/lat}}$  must be greater than  $10^5$  to significantly increase bulk diffusivities relative to lattice diffusivities. Moreover, the difference between bulk and lattice diffusivities decreases with increasing temperature, suggesting that bulk diffusivities are similar to lattice diffusivities in deformed mantle minerals.

Furthermore, Delon et al. (2018) demonstrated that a significant amount of He can be stored in grain boundaries (~22% at a grain size of 1 mm), enhancing the bulk diffusivities of mantle rocks. These results are highly dependent on grain size, implying that mantle deformation could significantly modify both the He storage capacity and bulk He diffusivities by grain size sensitive processes such as dynamic recrystallization (e.g., Kurz et al., 2009; Recanati et al., 2012). Indeed Kurz et al., (2009) reports a striking increase of He concentration as a function of the textures (from protogranular to mylonite) in rocks from St Paul Archipelago. However, the resulting dislocation density is not high enough to influence the storage and diffusive behavior of He in the mineral lattice of mantle rocks. Thus, the potential grain size reductions induced by dynamic recrystallization could result in a



redistribution of He between the mineral lattice and the grain boundary network to preserve a segregation factor of around  $10^5$  between grain boundaries and crystal lattice (Baxter et al., 2007; Delon et al., 2018). Two processes could play a role in such a He redistribution: (i) the diffusion of He through the crystal lattice and (ii) the motion of He-rich dislocations toward grain boundaries. At 800 °C, the velocity of He in olivine by diffusion process is around 50  $\text{nm}\cdot\text{s}^{-1}$ , significantly higher than the mobility of dislocations under stresses characteristic of deformed peridotites (i.e., stresses between 10 and 200 MPa; e.g., Gueguen and Darot, 1980), which is less than 10  $\text{nm}\cdot\text{s}^{-1}$  (Idrissi et al., 2016). Therefore, diffusion is the dominant process redistributing He between the olivine lattice and grain boundaries during plastic deformation. This process is very efficient since grain boundaries are equilibrated with olivine lattice in less than 3 hours at 800 °C at a grain size of 1 mm.

Nevertheless, the potential increased storage capacity of grain boundary network induced by dynamic recrystallization and grain size reduction does not imply an increase of bulk concentration, but only a redistribution of He between grain boundaries and the crystal lattice with respect to the segregation factor. To increase bulk concentrations, a homogenization must occur between the concentrations in grain boundaries (and thus in the crystal lattice to preserve the segregation factor) of rocks affected by dynamic recrystallization and those of nearby undeformed peridotites. To test this hypothesis in upper mantle rocks, we refer to Recanati et al. (2012), who studied the He abundance in protomylonites from a mantle shear zone (Josephine Peridotite, Oregon, USA) considered to be the remnant of a back-arc basin (e.g., Harper, 1984) or a fore-arc setting (e.g., Kelemen and Dick, 1995). The authors observed an abnormally high He concentration in a sample with a reduced grain size ( $\sim 285\ \mu\text{m}$ ) compared to adjacent rocks (average grain size of  $710\ \mu\text{m}$ ). They interpreted this high He concentration as resulting from a higher volume fraction of grain boundaries, suggesting that the sample was in equilibrium with coarser-grained peridotites (i.e., with similar He

concentrations in grain boundaries and the crystal lattice). To calculate the lattice ( $C^{LAT}$ ) and grain boundary ( $C^{GB}$ ) concentrations in these two rocks of different grain size, we perform a mass balance calculation by considering that the total He amount is equal to the combined amount of He stored in the crystal lattice and in grain boundaries. Based on the segregation factor between grain boundaries and the crystal lattice ( $s$ ), and the volume fraction of grain boundaries ( $v^{GB}$ ), we obtain:

$$C^{LAT} = \frac{C^{bulk}}{1 + sv^{GB}} \quad . \quad (5)$$

The value of  $s$  is taken as  $10^5$ , as observed by Baxter et al. (2007) in diopside and suggested by Delon et al. (2018) in olivine, and  $v^{GB} = 2.84 \delta/d$  with  $\delta = 0.75$  nm being the grain boundary width and  $d$  the grain size of the sample (Hiraga and Kohlstedt, 2009). We obtain  $C^{LAT} = 1.69 \pm 0.40 \times 10^{-12}$  mol·g<sup>-1</sup> for protomylonites with a grain size of 710  $\mu$ m and  $C^{LAT} = 2.98 \pm 0.20 \times 10^{-12}$  mol·g<sup>-1</sup> for the sample with a grain size of 285  $\mu$ m (for respective  $C^{bulk}$  values of  $2.20 \pm 0.52 \times 10^{-12}$  and  $5.20 \pm 0.35 \times 10^{-12}$  mol·g<sup>-1</sup>). Thus, the crystal lattice of the sample with a reduced grain size is enriched in He by almost a factor of two compared to the other samples, suggesting that dynamic recrystallization followed by homogenization with nearby rocks is not the sole mechanism responsible for the observed He enrichment. Even if this process can enhance bulk concentrations, a value of  $s$  around  $10^6$  is required to observe the increased concentration reported by Recanati et al. (2012). Instead, fluid percolation coupled with deformation could better explain the observed He enrichment. Indeed, fluid circulation is expected in back-arc basins and fore-arc settings, and it is reasonable to assume that this circulation occurs preferentially in deformed zones where percolation is easier due to the higher volume fraction of grain boundaries.

## 5. Conclusions

The diffusivities we obtained on three deformed samples and one undeformed sample allow new constraints on He storage and mobility in polycrystalline rocks.

- Diffusivities cannot be explained by a single linear regression, suggesting that they do not follow a single Arrhenius law in deformed polycrystalline forsterite. However, each step heating cycle can be fitted by several linear regressions depending on the temperature range (and constrained by a *F*-test), highlighting that diffusivities follow Arrhenius law over limited temperature ranges. Thus, the diffusive behavior of He in deformed polycrystalline forsterite is complex due to the competition of several diffusion mechanisms that are preferentially expressed in different temperature ranges. These different diffusion mechanisms are related to various storage sites since (i) the transitions between the temperature ranges where different diffusion mechanisms are expressed were different between cycles and samples, and (ii) the calculated  $E_a$  show large variations within individual cycles.
- By comparison with literature data, we identified different diffusion mechanisms that were expressed for each linear regression: (i) the LAT-high mechanism (i.e., diffusion in Mg vacancies), (ii) the LAT-high + LAT-low mechanisms (i.e., the co-governance of diffusion in Mg vacancies and interstitial sites), (iii) the LAT + GB (i.e., the co-governance of diffusion in the crystal lattice and along grain boundaries), and (iv) surface diffusion. Moreover, we observed a new diffusion mechanism in deformed forsterite, interpreted as the LAT + DIS mechanisms (i.e., the co-governance of diffusion in the crystal lattice and along dislocations).
- We have refined grain boundary diffusion parameters for He in polycrystalline olivine:  $E_a = 36 \pm 9 \text{ kJ}\cdot\text{mol}^{-1}$  and  $D_0 = 10^{-10.57 \pm 0.58} \text{ m}^2\cdot\text{s}^{-1}$ . Based on our results and literature data, we have refined those of He diffusion in Mg vacancies ( $E_a = 173 \pm 14 \text{ kJ}\cdot\text{mol}^{-1}$  and  $D_0 = 10^{-5.07 \pm 1.25} \text{ m}^2\cdot\text{s}^{-1}$ ) and in interstitial sites ( $E_a = 89 \pm 7 \text{ kJ}\cdot\text{mol}^{-1}$  and  $D_0 = 10^{-8.95 \pm 1.16} \text{ m}^2\cdot\text{s}^{-1}$ ).

Furthermore, we report  $E_a = 56 \pm 1 \text{ kJ}\cdot\text{mol}^{-1}$  and  $D_0 = 10^{-9.97 \pm 0.37} \text{ m}^2\cdot\text{s}^{-1}$  for He diffusion along dislocations.

- By applying these results to Earth's upper mantle, we showed that only a small fraction of He is stored along dislocations in the crystal lattice ( $<1.2\%$ ), which is negligible compared to the He fraction stored in grain boundaries ( $\sim 22\%$  for a grain size of 1 mm; Delon et al., 2018). Thus, the presence of He along dislocations does not strongly influence bulk diffusivities, which are very close to lattice diffusivities, and only the existence of a significant amount of He in grain boundaries could enhance the bulk diffusivities of mantle rocks. Nevertheless, potential grain size reduction induced by dynamic recrystallization would involve a redistribution of He between the crystal lattice and grain boundaries, which can increase bulk concentrations upon re-equilibration of grain boundaries in deformed rocks with those in nearby undeformed peridotites, thus enhancing bulk He diffusivities.

### *Acknowledgements*

This paper is dedicated to the memory of Pete Burnard (1965-2015), as the initiator of this project, our priceless colleague, and friend. The authors thank L. Zimmermann for his help on He analyses and D.V. Bekaert and M.W. Broadley for advice and assistance on the furnace. We are also grateful to M. Laumonier for his contribution to the piston cylinder experiments, J. Charreau for help with the  $F$ -tests, F. Barou for his help with SEM-EBSD analyses, and C. Nevado and D. Delmas for providing high-quality thin sections for SEM and TEM analyses. The TEM and EBSD-SEM national facilities in Lille and Montpellier are both supported by the Institut National de Sciences de l'Univers (INSU) du Centre National de la Recherche Scientifique (CNRS, France). The EBSD-SEM facility in Montpellier and TEM facility in Lille are also supported by the Conseil Régional Occitanie and by the Conseil Régional

Hauts-de-France (France), respectively. This study was supported by the JSPS KAKENHI Grant Number JP18K03799 to S. K. and Earthquake Research Institute's cooperative research program, 2016-B-05. M.A. Bouhifd acknowledges the support of the Labex ClerVolc (this is laboratory of Excellence ClerVolc contribution number 385). This study was mainly financed by l'Agence Nationale de la Recherche through grant ANR INDIGO (ANR-14-CE33-0011). This is CRPG contribution n° 2703.

#### *Research data*

Original data of this study are available in the supplementary file.

#### *References*

- Akaogi, M., Ito, E., and Navrotsky, A. (1989). Olivine-modified spinel-spinel transitions in the system  $\text{Mg}_2\text{SiO}_4\text{-Fe}_2\text{SiO}_4$ : Calorimetric measurements, thermochemical calculation, and geophysical application. *Journal of Geophysical Research: Solid Earth*, **94**(B11), 15671–15685.
- Allègre, C. J. (1987). Isotope geodynamics. *Earth and Planetary Science Letters*, **86**(2–4), 175–203.
- Andrault, D., Bouhifd, M. A., Itie, J. P., and Richet, P. (1995). Compression and amorphization of  $(\text{Mg, Fe})_2\text{SiO}_4$  olivines: an X-ray diffraction study up to 70 GPa. *Physics and Chemistry of Minerals*, **22**(2), 99–107.
- Barfod, D. N., Ballentine, C. J., Halliday, A. N., and Fitton, J. G. (1999). Noble gases in the Cameroon line and the He, Ne, and Ar isotopic compositions of high  $\mu$  (HIMU) mantle. *Journal of Geophysical Research: Solid Earth*, **104**(B12), 29509–29527.
- Baxter, E. F., Clay, P. L., Kelley, S. P., Watson, E. B., Cherniak, D. J., and Thomas, J. B. (2006). Two diffusive pathways for argon in quartz and feldspar. *Geochimica et*

668 *Cosmochimica Acta Supplement*, 70, A41–A41.

669 Baxter, E. F., Asimow, P. D., and Farley, K. A. (2007). Grain boundary partitioning of Ar and  
670 He. *Geochimica et Cosmochimica Acta*, 71(2), 434–451.  
671 <https://doi.org/10.1016/j.gca.2006.09.011>

672 Bekaert, D. V, Broadley, M. W., Delarue, F.,  
673 Avice, G., Robert, F., and Marty, B. (2018). Archean kerogen as a new tracer of  
674 atmospheric evolution: Implications for dating the widespread nature of early life.  
*Science Advances*, 4(2), eaar2091. <https://doi.org/10.1126/sciadv.aar2091>

675 Blard, P.-H., Puchol, N., and Farley, K. A. (2008). Constraints on the loss of matrix-sited  
676 helium during vacuum crushing of mafic phenocrysts. *Geochimica et Cosmochimica*  
677 *Acta*, 72, 3788–3803. <https://doi.org/10.1016/j.gca.2008.05.044>

678 Bouhifd, M. A., Jephcoat, A. P., Heber, V. S., and Kelley, S. P. (2013). Helium in Earth’s  
679 early core. *Nature Geoscience*, 6(11), 982.

680 Box, G. E. P. (1953). Non-normality and tests on variances. *Biometrika*, 40(3/4), 318–335.

681 Burnard, P., Demouchy, S., Delon, R., Arnaud, N. O., Marrocchi, Y., Cordier, P., and Addad,  
682 A. (2015). The role of grain boundaries in the storage and transport of noble gases in the  
683 mantle. *Earth and Planetary Science Letters*, 430, 260–270.  
684 <https://doi.org/10.1016/j.epsl.2015.08.024>

685 Cassata, W. S., Renne, P. R., and Shuster, D. L. (2011). Argon diffusion in pyroxenes:  
686 Implications for thermochronometry and mantle degassing. *Earth and Planetary Science*  
687 *Letters*, 304(3–4), 407–416. <https://doi.org/10.1016/j.epsl.2011.02.019>

688 Chakraborty, S. (1997). Rates and mechanisms of Fe-Mg interdiffusion in olivine at 980–  
689 1300 C. *Journal of Geophysical Research: Solid Earth*, 102(B6), 12317–12331.

690 Chakraborty, S. (2008). Diffusion in Solid Silicates: A Tool to Track Timescales of Processes  
691 Comes of Age. *Annual Review of Earth and Planetary Sciences*, 36(1), 153–190.  
692 <https://doi.org/10.1146/annurev.earth.36.031207.124125>

693 Cherniak, D. J., and Watson, E. B. (2012). Diffusion of helium in olivine at 1atm and 2.7GPa.  
694 *Geochimica et Cosmochimica Acta*, 84, 269–279.  
695 <https://doi.org/10.1016/j.gca.2012.01.042>

696 Chow, G. C. (1960). Tests of equality between sets of coefficients in two linear regressions.  
697 *Econometrica: Journal of the Econometric Society*, 591–605.

698 Clay, P. L., Baxter, E. F., Cherniak, D. J., Kelley, S. P., Thomas, J. B., and Watson, E. B.  
699 (2010). Two diffusion pathways in quartz: a combined UV-laser and RBS study.  
700 *Geochimica et Cosmochimica Acta*, 74(20), 5906–5925.

701 Coltice, N., Moreira, M., Hernlund, J., and Labrosse, S. (2011). Crystallization of a basal  
702 magma ocean recorded by helium and neon. *Earth and Planetary Science Letters*,  
703 308(1), 193–199.

704 Costa, F., and Chakraborty, S. (2008). The effect of water on Si and O diffusion rates in  
705 olivine and implications for transport properties and processes in the upper mantle.  
706 *Physics of the Earth and Planetary Interiors*, 166(1–2), 11–29.

707 Crank, J. (1975). *The Mathematics of Diffusion: 2d Ed.* Clarendon Press.

708 Delon, R., Demouchy, S., Marrocchi, Y., Bouhifd, M. A., Barou, F., Cordier, P., Addad, A.,  
709 Burnard, P. G. (2018). Helium incorporation and diffusion in polycrystalline olivine.  
710 *Chemical Geology*, 488(1), 105–124. <https://doi.org/10.1016/j.chemgeo.2018.04.013>

711 Delon, R., Demouchy, S., Marrocchi, Y., Bouhifd, M. A., Cordier, P., Addad, A., and  
712 Burnard, P. G. (2019). Argon storage and diffusion in Earth’s upper mantle. *Geochimica*  
713 *et Cosmochimica Acta*. <https://doi.org/10.1016/j.gca.2019.03.007>

714 Demouchy, S. (2010). Diffusion of hydrogen in olivine grain boundaries and implications for  
715 the survival of water-rich zones in the Earth’s mantle. *Earth and Planetary Science*  
716 *Letters*, 295(1–2), 305–313. <https://doi.org/10.1016/j.epsl.2010.04.019>

717 Demouchy, S., Tommasi, A., Barou, F., Mainprice, D., and Cordier, P. (2012). Deformation

of olivine in torsion under hydrous conditions. *Physics of the Earth and Planetary Interiors*, 202, 56–70.

Demouchy, S., Mussi, A., Barou, F., Tommasi, A., and Cordier, P. (2014). Viscoplasticity of polycrystalline olivine experimentally deformed at high pressure and 900 C. *Tectonophysics*, 623, 123–135. Dohmen, R. (2008). A new experimental thin film approach to study mobility and partitioning of elements in grain boundaries: Fe-Mg exchange between olivines mediated by transport through an inert grain boundary. *American Mineralogist*, 93(5–6), 863–874. <https://doi.org/10.2138/am.2008.2671>

Dohmen, R., and Chakraborty, S. (2007). Fe–Mg diffusion in olivine II: point defect chemistry, change of diffusion mechanisms and a model for calculation of diffusion coefficients in natural olivine. *Physics and Chemistry of Minerals*, 34(6), 409–430.

Dohmen, R., and Milke, R. (2010). Diffusion in Polycrystalline Materials: Grain Boundaries, Mathematical Models, and Experimental Data. *Reviews in Mineralogy and Geochemistry*, 72(1), 921–970. <https://doi.org/10.2138/rmg.2010.72.21>

Dohmen, R., Chakraborty, S., and Becker, H. (2002). Si and O diffusion in olivine and implications for characterizing plastic flow in the mantle. *Geophysical Research Letters*, 29(21), 21–26. Dunlap, W. J., and Kronenberg, A. (2001). Argon loss during deformation of micas: constraints from laboratory deformation experiments. *Contributions to Mineralogy and Petrology*, 141(2), 174–185.

Durinck, J., Carrez, P., and Cordier, P. (2007). Application of the Peierls-Nabarro model to dislocations in forsterite. *European Journal of Mineralogy*, 19(5), 631–639.

Farla, R.J.M., Kokkonen, H., Fitz Gerald, J.D., Barnhoorn, A., Faul, U.H., Jackson, I., 2010. Dislocation recovery in fine-grained polycrystalline olivine. *Phys Chem Minerals* 38, 363–377.

Farley, K. A., Basu, A. R., and Nilsson, K. (1991). Geochemistry and isotopic composition of



743       Guadalupe Island lavas and ultramafic xenoliths. *Eos, Trans. Am. Geophys. Union*,  
744       72(500), 2509–2517.

745   Fechtig, H., and Kalbitzer, S. (1966). The diffusion of argon in potassium-bearing solids. In  
746       *Potassium argon dating* (pp. 68–107). Springer.

747   Futagami, T., Ozima, M., Nagai, S., and Aoki, Y. (1993). Experiments on thermal release of  
748       implanted noble gases from minerals and their implications for noble gases in lunar soil  
749       grains. *Geochimica et Cosmochimica Acta*, 57(13), 3177–3194.  
750       [https://doi.org/10.1016/0016-7037\(93\)90302-D](https://doi.org/10.1016/0016-7037(93)90302-D)

751   Gasc, J., Demouchy, S., Barou, F., Koizumi, S., and Cordier, P. (2019). Creep mechanisms in  
752       the lithospheric mantle inferred from deformation of iron-free forsterite aggregates at  
753       900–1200° C. *Tectonophysics*. <https://doi.org/10.1016/j.tecto.2019.04.009>

754   Gérard, O., and Jaoul, O. (1989) Oxygen diffusion in San Carlos olivine. *Journal of*  
755       *Geophysical Research*, 94(B4), 4119–4128. <https://doi.org/10.1029/JB094iB04p04119>.

756   German, R. (2014). *Sintering: from empirical observations to scientific principles*.  
757       Butterworth-Heinemann.

758   Gueguen, Y., and Darot, M. (1980). Microstructures and stresses in naturally deformed  
759       peridotites. In *Tectonic Stresses in the Alpine-Mediterranean Region* (pp. 159–172).  
760       Springer.

761   Hahs-Vaughn, D. L., and Lomax, R. G. (2013). *Statistical concepts: A second course*.  
762       Routledge.

763   Ham, R. K. (1961). The determination of dislocation densities in thin films. *Philosophical*  
764       *Magazine*, 6(69), 1183–1184.

765   Harper, G. D. (1984). The Josephine ophiolite, northwestern California. *Geological Society of*  
766       *America Bulletin*, 95(9), 1009–1026.

767   Harrison, L. G. (1961). Influence of dislocations on diffusion kinetics in solids with particular

reference to the alkali halides. *Transactions of the Faraday Society*, 57, 1191.  
<https://doi.org/10.1039/tf9615701191>

Harrison, T. M., and Lovera, O. M. (2014). The multi-diffusion domain model: past, present  
 and future. *Geological Society, London, Special Publications*, 378(1), 91–106.

Hart, E. W. (1957). On the role of dislocations in bulk diffusion. *Acta Metallurgica*, 5(10),  
 597. [https://doi.org/http://dx.doi.org/10.1016/0001-6160\(57\)90127-X](https://doi.org/http://dx.doi.org/10.1016/0001-6160(57)90127-X)

Heber, V. S., Brooker, R. A., Kelley, S. P., and Wood, B. J. (2007). Crystal–melt partitioning  
 of noble gases (helium, neon, argon, krypton, and xenon) for olivine and clinopyroxene.  
*Geochimica et Cosmochimica Acta*, 71(4), 1041–1061.

Heizler, M. T., Ralser, S., and Karlstrom, K. E. (1997). Late Proterozoic (Grenville?)  
 deformation in central New Mexico determined from single-crystal muscovite  
 40Ar/39Ar age spectra. *Precambrian Research*, 84(1–2), 1–15.

Hilton, D. R., McMurtry, G. M., and Kreulen, R. (1997). Evidence for extensive degassing of  
 the Hawaiian mantle plume from helium-carbon relationships at Kilauea volcano.  
*Geophysical Research Letters*, 24(23), 3065–3068.

Hiraga, T., and Kohlstedt, D. L. (2009). Systematic distribution of incompatible elements in  
 mantle peridotite: Importance of intra- and inter-granular melt-like components.  
*Contributions to Mineralogy and Petrology*, 158(2), 149–167.  
<https://doi.org/10.1007/s00410-009-0375-8>

Hiyagon, H., Ozima, M., Marty, B., Zashu, S., and Sakai, H. (1992). Noble gases in  
 submarine glasses from mid-oceanic ridges and Loihi seamount: constraints on the early  
 history of the Earth. *Geochimica et Cosmochimica Acta*, 56(3), 1301–1316.

Holland, G., & Ballentine, C. J. (2006). Seawater subduction controls the heavy noble gas  
 composition of the mantle. *Nature*, 441(7090), 186.

Holzapel, C., Chakraborty, S., Rubie, D. C., and Frost, D. J. (2007). Effect of pressure on

793 Fe–Mg, Ni and Mn diffusion in  $(\text{Fe}_x\text{Mg}_{1-x})_2\text{SiO}_4$  olivine. *Physics of the Earth and*  
794 *Planetary Interiors*, 162(3–4), 186–198.

795 Honda, M., McDougall, I., Patterson, D. B., Doulgeris, A., and Clague, D. A. (1993). Noble  
796 gases in submarine pillow basalt glasses from Loihi and Kilauea, Hawaii: a solar  
797 component in the Earth. *Geochimica et Cosmochimica Acta*, 57(4), 859–874.

798 Hull, D., Bacon, D.J. (1989). Introduction to dislocation, International Series on Materials  
799 Science and Technology. *Pergamon press*, New York.

800 Idrissi, H., Bollinger, C., Boioli, F., Schryvers, D., and Cordier, P. (2016). Low-temperature  
801 plasticity of olivine revisited with in situ TEM nanomechanical testing. *Science*  
802 *Advances*, 2(3), e1501671.

803 Jackson, C. R. M., Parman, S. W., Kelley, S. P., and Cooper, R. F. (2013). Constraints on  
804 light noble gas partitioning at the conditions of spinel-peridotite melting. *Earth and*  
805 *Planetary Science Letters*, 384, 178–187.

806 Jaoul, O., Houlier, B., Cheraghmakani, M., Pichon, R., and Liebermann, R. C. (1987).  
807 Surface destabilization and laboratory-induced non-stoichiometry in San Carlos olivine.  
808 *Physics and Chemistry of Minerals*, 15(1), 41–53.

809 Joesten, R. (1991). Grain-boundary diffusion kinetics in silicate and oxide minerals. In  
810 *Diffusion, atomic ordering, and mass transport* (pp. 345–395). Springer.

811 Kaneoka, I., Takaoka, N., and Clague, D. A. (1983). Noble gas systematics for coexisting  
812 glass and olivine crystals in basalts and dunite xenoliths from Loihi Seamount. *Earth and*  
813 *Planetary Science Letters*, 66, 427–437.

814 Kelemen, P. B., and Dick, H. J. B. (1995). Focused melt flow and localized deformation in  
815 the upper mantle: Juxtaposition of replacive dunite and ductile shear zones in the  
816 Josephine peridotite, SW Oregon. *Journal of Geophysical Research: Solid Earth*,  
817 100(B1), 423–438.

818 Kelley, S., Baxter, E., Cherniak, D., Clay, P., Thomas, J., and Watson, E. (2008). Two  
 819 diffusion mechanisms for Argon in K-feldspar? *Geochimica et Cosmochimica Acta*  
 820 *Supplement* (Vol. 72).

821 Kendrick, M. A., Scambelluri, M., Hermann, J., & Padrón-Navarta, J. A. (2018). Halogens  
 822 and noble gases in serpentinites and secondary peridotites: Implications for seawater  
 823 subduction and the origin of mantle neon. *Geochimica et Cosmochimica Acta*, 235, 285–  
 824 304. <https://doi.org/10.1016/j.gca.2018.03.024>

825 Kish, L., and Cuney, M. (1981). Uraninite-albite veins from the Mistamisk Valley of the  
 826 Labrador Trough, Quebec. *Mineralogical Magazine*, 44(336), 471–483.

827 Koizumi, S., Hiraga, T., Tachibana, C., Tasaka, M., Miyazaki, T., Kobayashi, T., Takamasa,  
 828 A., Ohashi, N., and Sano, S. (2010). Synthesis of highly dense and fine-grained  
 829 aggregates of mantle composites by vacuum sintering of nano-sized mineral powders.  
 830 *Physics and Chemistry of Minerals*, 37(8), 505–518. [https://doi.org/10.1007/s00269-009-](https://doi.org/10.1007/s00269-009-0350-y)  
 831 0350-y

832 Kramar, N., Cosca, M. A., and Hunziker, J. C. (2001). Heterogeneous  $^{40}\text{Ar}^*$  distributions in  
 833 naturally deformed muscovite: in situ UV-laser ablation evidence for microstructurally  
 834 controlled intragrain diffusion. *Earth and Planetary Science Letters*, 192(3), 377–388.

835 Kurz, M.D., Jenkins, W.J., Hart, S.R. (1982). Helium isotopic systematics of oceanic islands  
 836 and mantle heterogeneity. *Nature*, 297, 43–47.

837 Kurz, M. D., Jenkins, W. J., Hart, S. R., and Clague, D. (1983). Helium isotopic variations in  
 838 volcanic rocks from Loihi Seamount and the Island of Hawaii. *Earth and Planetary*  
 839 *Science Letters*, 66, 388–406.

840 Kurz, M. D., Warren, J. M., & Curtice, J. (2009). Mantle deformation and noble gases :  
 841 Helium and neon in oceanic mylonites. *Chemical Geology*, 266(1–2), 10–18.  
 842 <https://doi.org/10.1016/j.chemgeo.2008.12.018>

843 Labrosse, S., Hernlund, J. W., and Coltice, N. (2007). A crystallizing dense magma ocean at  
 844 the base of the Earth's mantle. *Nature*, 450(7171), 866.

845 Lee, J. K. W. (1995). Multipath diffusion in geochronology. *Contributions to Mineralogy and*  
 846 *Petrology*, 120(1), 60–82. <https://doi.org/10.1007/BF00311008>

847 Legros, M., Dehm, G., Artz, E. and Balk, T.J. (2008) Observation of giant diffusivity along  
 848 dislocation cores. *Science*, 319, 1646-1649. <https://doi.org/10.1126/science.1151771>

849 Lovera, O. M. (1992). Computer programs to model  $^{40}\text{Ar}/^{39}\text{Ar}$  diffusion data from  
 850 multidomain samples. *Computers and Geosciences*, 18(7), 789–813.

851 Lovera, O. M., Richter, F. M., and Harrison, T. M. (1989). The  $^{40}\text{Ar}/^{39}\text{Ar}$  thermochronometry  
 852 for slowly cooled samples having a distribution of diffusion domain sizes. *Journal of*  
 853 *Geophysical Research: Solid Earth*, 94(B12), 17917–17935.  
 854 <https://doi.org/10.1029/JB094iB12p17917>

855 Mackwell, S. J., and Kohlstedt, D. L. (1990). Diffusion of hydrogen in olivine: implications  
 856 for water in the mantle. *Journal of Geophysical Research: Solid Earth*, 95(B4), 5079–  
 857 5088.

858 Mahendran, S., Carrez, P., Groh, S., and Cordier, P. (2017). Dislocation modelling in  
 859  $\text{Mg}_2\text{SiO}_4$  forsterite: an atomic-scale study based on the THB1 potential. *Modelling and*  
 860 *Simulation in Materials Science and Engineering*, 25(5), 54002.

861 Marrocchelli, D., Sun, L. and Yildiz, B. (2015) Dislocations in  $\text{SrTiO}_3$ : Easy To Reduce but  
 862 Not so Fast for Oxygen Transport. *Journal of the American Chemical Society*, 137,  
 863 4735-4748. Doi: 10.1021/ja513176u.

864 Matsuda, J., Matsumoto, T., Sumino, H., Nagao, K., Yamamoto, J., Miura, Y., Sano, Y.  
 865 (2002). The  $3\text{He}/4\text{He}$  ratio of new internal He Standard of Japan (HESJ). *Geochemical*  
 866 *Journal*, 36(2), 191–195. <https://doi.org/10.2343/geochemj.36.191>

867 McDougall, I., and Harrison, T. M. (1999). Geochronology and Thermochronology by the

868  $^{40}\text{Ar}/^{39}\text{Ar}$  Method.

869 Mei, S., and Kohlstedt, D. L. (2000). Influence of water on plastic deformation of olivine  
870 aggregates: 1. Diffusion creep regime. *Journal of Geophysical Research: Solid Earth*,  
871 *105*(B9), 21457–21469.

872 Mishin, Y., and Herzig, C. (1995). Diffusion in fine-grained materials: Theoretical aspects  
873 and experimental possibilities. *Nanostructured Materials*, *6*(5–8), 859–862.  
874 [https://doi.org/10.1016/0965-9773\(95\)00195-6](https://doi.org/10.1016/0965-9773(95)00195-6)

875 Mishin, Y., and Herzig, C. (1999). Grain boundary diffusion: recent progress and future  
876 research. *Materials Science and Engineering: A*, *260*(1–2), 55–71.  
877 [https://doi.org/10.1016/S0921-5093\(98\)00978-2](https://doi.org/10.1016/S0921-5093(98)00978-2)

878 Moreira, M. (2013). Noble gas constraints on the origin and evolution of Earth’s volatiles.  
879 *Geochemical Perspectives*, *2*(2), 229–230.

880 Moreira, M. A., and Kurz, M. D. (2013). Noble gases as tracers of mantle processes and  
881 magmatic degassing. In *The Noble Gases as Geochemical Tracers* (pp. 371–391).  
882 Springer.

883 Moreira, M., and Raquin, A. (2007). The origin of rare gases on Earth: The noble gas  
884 “subduction barrier” revisited. *Comptes Rendus Geoscience*, *339*(14), 937–945.

885 Moreira, M., Doucelance, R., Kurz, M. D., Dupré, B., and Allègre, C. J. (1999). Helium and  
886 lead isotope geochemistry of the Azores Archipelago. *Earth and Planetary Science*  
887 *Letters*, *169*(1), 189–205.

888 Mulch, A., Cosca, M., and Handy, M. (2002). In-situ UV-laser  
889  $^{40}\text{Ar}/^{39}\text{Ar}$  geochronology of a micaceous mylonite: an example of defect-enhanced  
889 argon loss. *Contributions to Mineralogy and Petrology*, *142*(6), 738–752.

890 Nakamura, A., & Schmalzried, H. (1984). On the  $\text{Fe}^{2+}$ – $\text{Mg}^{2+}$ -Interdiffusion in Olivine (II).  
891 *Berichte Der Bunsengesellschaft Für Physikalische Chemie*, *88*(2), 140–145.

892 Padrón-Navarta, J. A., Hermann, J., and O’Neill, H. S. C. (2014). Site-specific hydrogen

diffusion rates in forsterite. *Earth and Planetary Science Letters*, 392, 100–112.

Parai, R., & Mukhopadhyay, S. (2015). The evolution of MORB and plume mantle volatile budgets: Constraints from fission Xe isotopes in Southwest Indian Ridge basalts. *Geochemistry Geophysics Geosystems*, 16(1), 719–735. <https://doi.org/10.1002/2014GC005566>

Paterson, M. S. (1990). Rock deformation experimentation. *The Brittle-Ductile Transition in Rocks*, 187–194.

Piazolo, S., La Fontaine, A., Trimby, P., Harley, S., Yang, L., Armstrong, R., and Cairney, J. M. (2016). Deformation-induced trace element redistribution in zircon revealed using atom probe tomography. *Nature Communications*, 7.

Pinilla, C., Davis, S. a., Scott, T. B., Allan, N. L., and Blundy, J. D. (2012). Interfacial storage of noble gases and other trace elements in magmatic systems. *Earth and Planetary Science Letters*, 319–320, 287–294. <https://doi.org/10.1016/j.epsl.2011.12.018>

Porcelli, D., and Halliday, A. N. (2001). The core as a possible source of mantle helium. *Earth and Planetary Science Letters*, 192(1), 45–56.

Recanati, A., Kurz, M. D., Warren, J. M., and Curtice, J. (2012). Helium distribution in a mantle shear zone from the Josephine Peridotite. *Earth and Planetary Science Letters*, 359, 162–172.

Reddy, S. M., Kelley, S. P., and Wheeler, J. (1996). A  $^{40}\text{Ar}/^{39}\text{Ar}$  laser probe study of micas from the Sesia Zone, Italian Alps: implications for metamorphic and deformation histories. *Journal of Metamorphic Geology*, 14(4), 493–508.

Reddy, S. M., Potts, G. J., Kelley, S. P., and Arnaud, N. O. (1999). The effects of deformation-induced microstructures on intragrain  $^{40}\text{Ar}/^{39}\text{Ar}$  ages in potassium feldspar. *Geology*, 27(4), 363–366.

Reddy, S. M., Potts, G. J., and Kelley, S. P. (2001).  $^{40}\text{Ar}/^{39}\text{Ar}$  ages in deformed potassium

918 feldspar: evidence of microstructural control on Ar isotope systematics. *Contributions to*  
 919 *Mineralogy and Petrology*, 141(2), 186–200. Reiners, P. W., and Farley, K. A. (1999).  
 920 Helium diffusion and (U-Th)/He thermochronometry of titanite. *Geochimica et*  
 921 *Cosmochimica Acta*, 63(22), 3845–3859.  
 922 <https://doi.org/10.1180/minmag.1998.62A.2.318>  
 923 Reiners, P. W., Spell, T. L., Nicolescu, S., and Zanetti, K. A. (2004). Zircon (U-Th)/He  
 924 thermochronometry: He diffusion and comparisons with  $^{40}\text{Ar}/^{39}\text{Ar}$  dating. *Geochimica*  
 925 *et Cosmochimica Acta*, 68(8), 1857–1887. <https://doi.org/10.1016/j.gca.2003.10.021>  
 926 Rison, W., and Craig, H. (1983). Helium isotopes and mantle volatiles in Loihi Seamount and  
 927 Hawaiian Island basalts and xenoliths. *Earth and Planetary Science Letters*, 66, 407–  
 928 426.  
 929 Smye, A. J., Jackson, C. R. M., Konrad-Schmolke, M., Hesse, M. A., Parman, S. W., Shuster,  
 930 D. L., and Ballentine, C. J. (2017). Noble gases recycled into the mantle through cold  
 931 subduction zones. *Earth and Planetary Science Letters*, 471, 65–73.  
 932 Starkey, N. A., Stuart, F. M., Ellam, R. M., Fitton, J. G., Basu, S., & Larsen, L. M. (2009).  
 933 Helium isotopes in early Iceland plume picrites: Constraints on the composition of high  
 934  $^3\text{He}/^4\text{He}$  mantle. *Earth and Planetary Science Letters*, 277(1–2), 91–100.  
 935 <https://doi.org/10.1016/j.epsl.2008.10.007>  
 936 Staudacher, T., and Allègre, C. J. (1988). Recycling of oceanic crust and sediments: the noble  
 937 gas subduction barrier. *Earth and Planetary Science Letters*, 89(2), 173–183.  
 938 Stuart, F. M., Lass-Evans, S., Fitton, J. G., & Ellam, R. M. (2003). High  $^3\text{He}/^4\text{He}$  ratios in  
 939 picritic basalts from Baffin Island and the role of a mixed reservoir in mantle plumes.  
 940 *Nature*, 424(6944), 57–59.  
 941 Thieme, M., Demouchy, S., Mainprice, D., Barou, F., and Cordier, P. (2018). Stress evolution  
 942 and associated microstructure during transient creep of olivine at 1000–1200° C. *Physics*



943        *of the Earth and Planetary Interiors*, 278, 34–46.

944    Thomas, J. B., Cherniak, D. J., and Watson, E. B. (2008). Lattice diffusion and solubility of  
945        argon in forsterite, enstatite, quartz and corundum. *Chemical Geology*, 253(1–2), 1–22.  
946        <https://doi.org/10.1016/j.chemgeo.2008.03.007>

947    Thoraval, C., and Demouchy, S. (2014). Numerical models of ionic diffusion in one and three  
948        dimensions: application to dehydration of mantle olivine. *Physics and Chemistry of*  
949        *Minerals*, 41(9), 709–723.

950    Tolstikhin, I., Kamensky, I., Tarakanov, S., Kramers, J., Pekala, M., Skiba, V., Gannibal, M.,  
951        Novikov, D. (2010). Noble gas isotope sites and mobility in mafic rocks and olivine.  
952        *Geochimica et Cosmochimica Acta*, 74(4), 1436–1447.  
953        <https://doi.org/10.1016/j.gca.2009.11.001>

954    Trull, T. W., and Kurz, M. D. (1993). Experimental measurements of <sup>3</sup>He and <sup>4</sup>He mobility in  
955        olivine and clinopyroxene at magmatic temperatures. *Geochimica et Cosmochimica*  
956        *Acta*, 57(6), 1313–1324. [https://doi.org/10.1016/0016-7037\(93\)90068-8](https://doi.org/10.1016/0016-7037(93)90068-8)

957    Valbracht, P. J., Staudacher, T., Malahoff, A., and Allègre, C. J. (1997). Noble gas  
958        systematics of deep rift zone glasses from Loihi Seamount, Hawaii. *Earth and Planetary*  
959        *Science Letters*, 150(3), 399–411.

960    Van Soest, M. C., Monteleone, B. D., Hodges, K. V, and Boyce, J. W. (2011). Laser depth  
961        profiling studies of helium diffusion in Durango fluorapatite. *Geochimica et*  
962        *Cosmochimica Acta*, 75(9), 2409–2419.

963    Wallis, D., Hansen, L. N., Tasaka, M., Kumamoto, K. M., Parsons, A. J., Lloyd, G. E.,  
964        Kohlstedt, A.J., Wilkinson, A. J. (2019). The impact of water on slip system activity in  
965        olivine and the formation of bimodal crystallographic preferred orientations. *Earth and*  
966        *Planetary Science Letters*, 508, 51–61.

967    Wang, K., Brodholt, J., and Lu, X. (2015). Helium diffusion in olivine based on first

- principles calculations. *Geochimica et Cosmochimica Acta*, 156, 145–153.
- Wartho, J.-A., Kelley, S. P., and Elphick, S. C. (2014). Ar diffusion and solubility measurements in plagioclases using the ultra-violet laser depth-profiling technique. *Geological Society, London, Special Publications*, 378(1), 137–154.
- Watson, E. B., and Cherniak, D. J. (2003). Lattice diffusion of Ar in quartz, with constraints on Ar solubility and evidence of nanopores. *Geochimica et Cosmochimica Acta*, 67(11), 2043–2062.
- Watson, E. B., Thomas, J. B., and Cherniak, D. J. (2007). <sup>40</sup>Ar retention in the terrestrial planets. *Nature*, 449(7160), 299.
- Wolfenstine, J. (1990) Effects of pipe diffusion on the creep behaviour of dry olivine. *Philosophical Magazine Letters*, 62, 233-238.  
<https://doi.org/10.1080/09500839008215128>
- Yurimoto, H., Morioka, M. and Nagasawa, H. (1992) Oxygen self-diffusion along high diffusivity paths in forsterite. *Geochemical Journal*, 26, 181-188.  
<https://doi.org/10.2343/geochemj.26.181>
- Zhao, Y. and-H., Ginsberg, S., & Kohlstedt, D. L. (2001). Experimental investigation on water solubility in olivine single crystal with different Fe content. *Acta Petrologica Sinica*, 17(1), 123–128.
- Zhao, Y. H., Zimmerman, M. E., & Kohlstedt, D. L. (2009). Effect of iron content on the creep behavior of olivine: 1. Anhydrous conditions. *Earth and Planetary Science Letters*, 287(1–2), 229–240. <https://doi.org/10.1016/j.epsl.2009.08.006>

*Figure captions*

Fig. 1. Schematic representation of diffusion mechanisms related to storage sites in polycrystalline rocks undergoing doping by diffusion (e.g., chemical flux). The kinetic regime represented here is the B-regime (following the classification of Harrison, 1961) to highlight the different diffusion rates related to each storage types (point defects, dislocations, grain boundaries). Dislocation forests are local entanglement of linear defects and dislocation cores are the distortion of the lattice (inducing an extra strain energy) around a dislocation (e.g., Hull and Bacon, 1984). An indicative scale is the cube edge = 10 nm.

Fig. 2. Experimental sample assembly for doping experiments in piston cylinder.

Fig. 3. SEM images of post-deformation pre-doping polycrystalline olivine (a) sample NF\_SM, which is the starting material (b) sample NF\_1200-1, (c) sample NF\_1050-1, and (d) sample NF\_950-1. TEM images of microstructures in post-deformation pre-doping polycrystalline olivine (e) sample NF\_1200-1 and (f–g) sample NF\_950-1.

Fig. 4. Arrhenius diagrams of He diffusion coefficients obtained from step heating analyses of (a) undeformed sample NF\_SM and deformed samples (b) NF\_950-1, (c) NF\_1050-1, and (d) NF\_1200-1. Multiple linear regressions were performed on each heating cycle, and the best-fit model for each cycle was selected based on the results of  $F$ -tests (see text and supplementary material). Gray dotted lines are the exceptions to  $F$ -tests, which were preferentially chosen to better fit the data (see text for more details). The numbers of the regressions correspond to the labeled data points in Fig. 5.

Fig. 5. Compilation of (a) the logarithm of the pre-exponential factors and (b) the activation energies for samples from this study. Results are compared with Ar surface diffusion

(Burnard et al., 2015), bulk He diffusion when lattice and grain boundary diffusion are expressed (LAT + GB; Burnard et al., 2015; Delon et al., 2018), bulk He lattice diffusion where diffusion in interstitial sites and Mg vacancies are expressed (LAT-high + LAT-low; Delon et al., 2018), and He diffusion in Mg vacancies (LAT-high; Delon et al., 2018). Grey points indicate data for the corresponding cycles that were reprocessed using three linear regressions instead of two (see text). The numbers of the data points correspond to the numbered linear regressions shown in Fig. 4.

Fig. 6. Arrhenius diagram of He grain boundary diffusion (reprocessed from Delon et al., 2018), diffusion in interstitial sites and Mg vacancies (data from this study and Delon et al., 2018), and combined diffusion in the crystal lattice and along dislocations (i.e., LAT + DIS mechanisms, this study).

Fig. 7. Bulk lattice diffusivities (black dotted lines) calculated from Eq. (3) as a function of temperature for different values of  $K^{\text{dis/lat}}$  and the maximum value of  $\rho$  in the Earth's mantle ( $10^{12} \text{ m}^{-2}$ ). Diffusion along dislocations (green line) and diffusion in interstitials (orange line) are shown for comparison.

#### *Table captions*

Table 1. Experimental conditions for deformation, doping, and step heating experiments. Average grain sizes were determined from SEM-EBSD maps.

Table 2. He diffusion parameters,  $\log(D_0/a^2)$  and  $E_a$ , obtained from each linear regression, which were defined using  $F$ -tests for each heating step cycle. Data from two cycles were

1041 reprocessed to fit the data using three linear regressions instead of two as we favored this  
1042 model instead of the results of the  $F$ -tests (see text for more details).

1043

1044 Table 3. Diffusion equations defining helium diffusion in polycrystalline olivine from this  
1045 study and Delon et al. (2018).

Table

Type of experiment	Temperature	Pressure	Duration	Strain	Sample	Mass	Average grain size
	°C	MPa		%		mg	μm
<i>Deformation experiments</i>							
Paterson Press	1200 ± 25	300 ± 10	3h03	10.0	NF_1200-1	–	3.1
Paterson Press	1050 ± 25	300 ± 10	3h31	10.4	NF_1050-1	–	2.9
Paterson Press	950 ± 25	300 ± 10	2h48	3.1	NF_950-1	–	2.7
<i>Doping experiments</i>							
Piston cylinder	1120 ± 20	1 000 ± 20	24 h	–	NF_SM	47	3.1
					Uraninite	16	–
Piston cylinder	1120 ± 20	1 000 ± 20	24 h	–	NF_1200-1	46	3.1
					Uraninite	11	–
Piston cylinder	1120 ± 20	1 000 ± 20	24 h	–	NF_1050-1	96	2.9
					Uraninite	10	–
Piston cylinder	1120 ± 20	1 000 ± 20	24 h	–	NF_950-1	69	2.7
					Uraninite	12	–
<i>Cycled step heating experiments</i>							
Helix MC	Every 50 or 100 °C	around 10 <sup>−12</sup>	30 min per step	–	NF_SM	9.3	3.1
	Cycle 1: 400-800 °C						
	Cycle 2: 600-650 °C						
	Cycle 3: 400-650 °C						
	Cycle 4: 650-1300 °C						
Helix MC	Every 50 or 100 °C	around 10 <sup>−12</sup>	30 min per step	–	NF_1200-1	8.0	3.1
	Cycle 1: 400-750 °C						
	Cycle 2: 500-1200 °C						
Helix MC	Every 50 or 100 °C	around 10 <sup>−12</sup>	30 min per step	–	NF_1050-1	8.8	2.9
	Cycle 1: 400-1100 °C						
	Cycle 2: 400-1000 °C						
Helix MC	Every 50 °C	around 10 <sup>−12</sup>	30 min per step	–	NF_950-1	3.6	2.7
	Cycle 1: 400-950 °C						
	Cycle 2: 400-1000 °C						

Table 1

Sample		Temperature range °C	Activation energy kJ.mol <sup>-1</sup>	Log( $D_0/a^2$ ) m <sup>2</sup> .s <sup>-1</sup> /m <sup>2</sup>
NF_SM	<i>Cycle 1</i>	401–556	6 ± 12	−9.44 ± 0.82
		602–805	146 ± 11	−0.89 ± 0.57
	<i>Cycle 1 (reprocessed)</i>	401–509	2 ± 24	−9.70 ± 1.70
		556–649	88 ± 8	−4.25 ± 0.47
		695–805	173 ± 17	0.50 ± 0.87
	<i>Cycle 2</i>	602–649	11	−8.22
	<i>Cycle 3</i>	509–649	89 ± 10	−3.80 ± 0.58
	<i>Cycle 4</i>	852–946	330 ± 29	7.98 ± 1.29
		993–1295	120 ± 8	−1.01 ± 0.29
NF_950-1	<i>Cycle 1</i>	447–649	10 ± 7	−5.47 ± 0.42
		695–946	89 ± 8	−1.45 ± 0.39
	<i>Cycle 2</i>	602–758	68 ± 6	−3.07 ± 0.36
		805–946	150 ± 1	1.0 ± 0.01
	<i>Cycle 2 (reprocessed)</i>	602–695	56 ± 1	−3.76 ± 0.02
		695–805	96 ± 3	−1.63 ± 0.17
		852–946	150 ± 1	1.00 ± 0.03
NF_1050-2	<i>Cycle 1</i>	401–602	3 ± 6	−5.52 ± 0.42
		649–805	22 ± 5	−4.64 ± 0.22
		852–993	77 ± 4	−1.82 ± 0.15
	<i>Cycle 2</i>	401–494	20 ± 16	−6.04 ± 1.18
		556–993	55 ± 2	−3.76 ± 0.13
NF_1200-1	<i>Cycle 1</i>	401–602	100 ± 6	−2.96 ± 0.41
		649–758	228 ± 1	4.45 ± 0.02
	<i>Cycle 2</i>	494–649	57 ± 2	−4.40 ± 0.14
		695–805	201 ± 2	3.29 ± 0.12
		899–1199	88 ± 1	−1.89 ± 0.06

N.B. Activation energies are calculated with  $a = 1$  m as activation energies do not depend on the value of  $a$  (see Burnard *et al.*, 2015 for further details)

*Table 2*

Diffusion mechanism	Formal notations	Diffusion equation	References
Diffusion via Mg vacancies	LAT-high	$D = 10^{-5.07 \pm 1.25} \exp [-(173,000 \pm 14,000)/RT]$	Delon et al., 2018 This study
Diffusion via interstitials	LAT-low	$D = 10^{-8.95 \pm 1.16} \exp [-(89,000 \pm 7,000)/RT]$	Delon et al., 2018 This study
Diffusion along dislocations	DIS	$D = 10^{-9.97 \pm 0.37} \exp [-(56,000 \pm 1,000)/RT]$	This study
Diffusion via grain boundaries	GB	$D = 10^{-10.57 \pm 0.58} \exp [-(36,000 \pm 9,000)/RT]$	Delon et al., 2018

*Table 3*



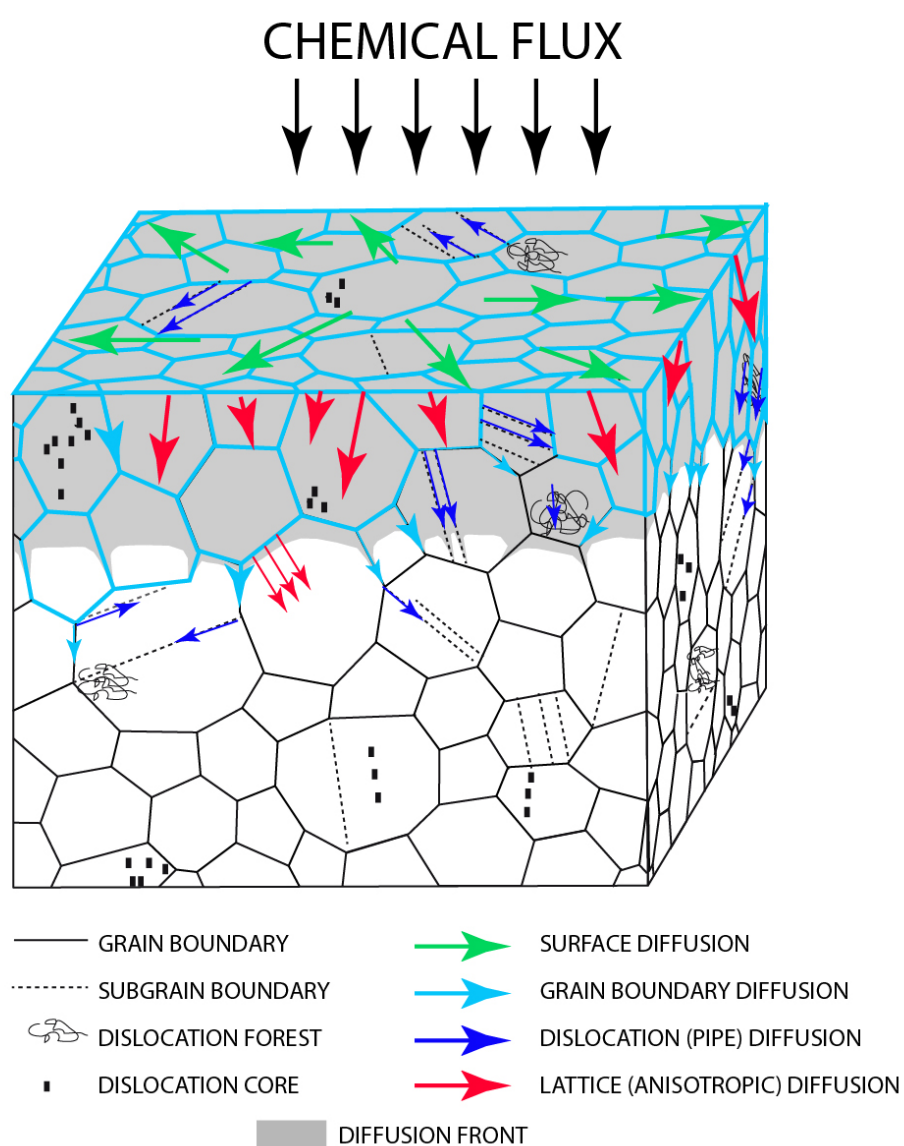
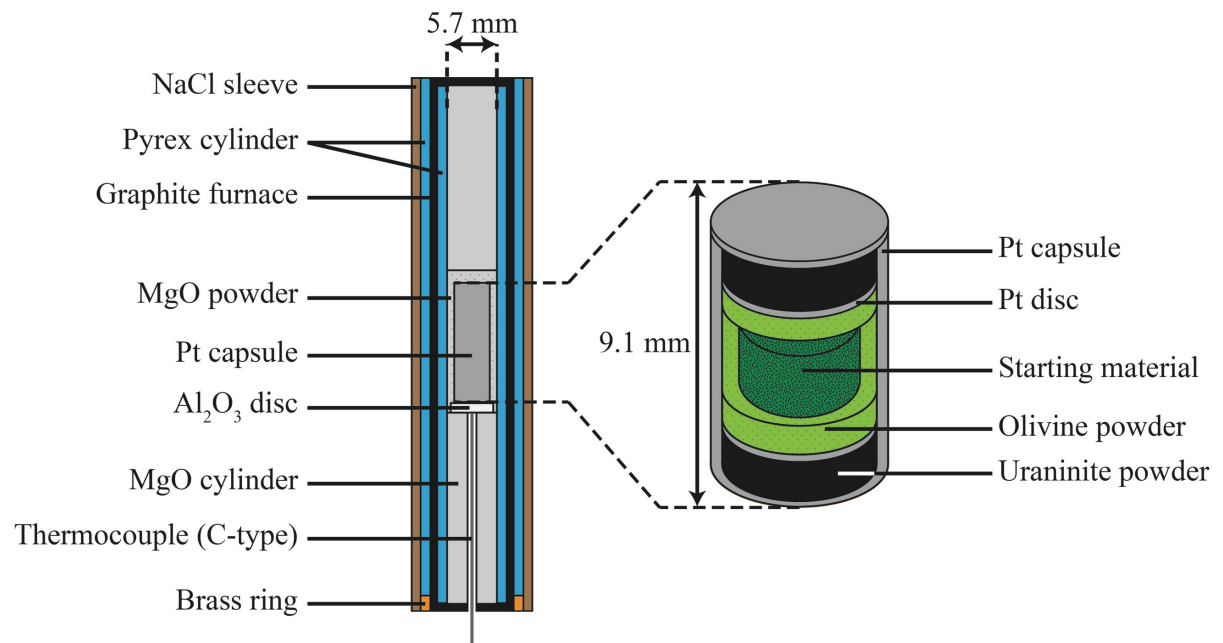


Figure 1



*Figure 2*

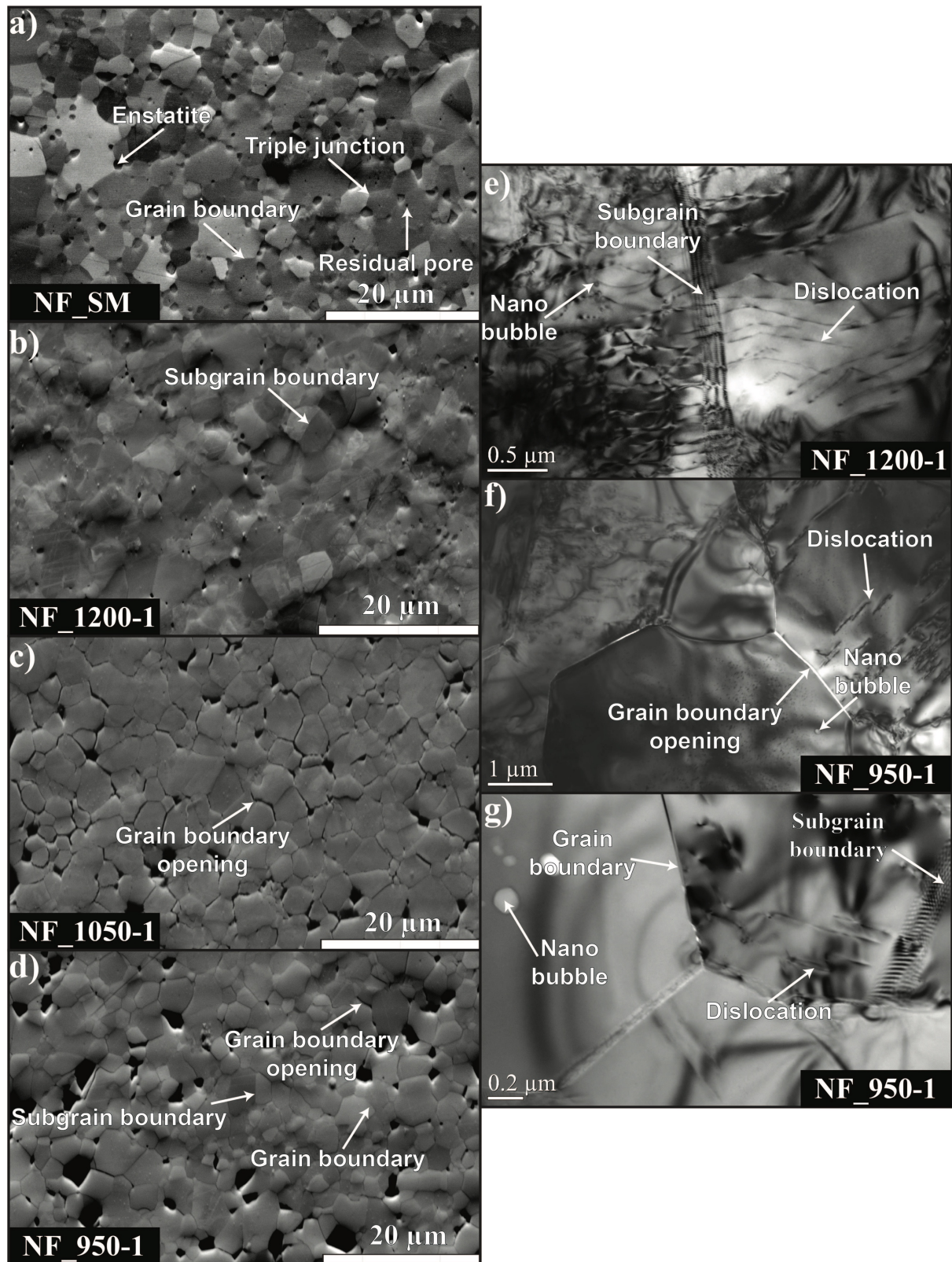


Figure 3

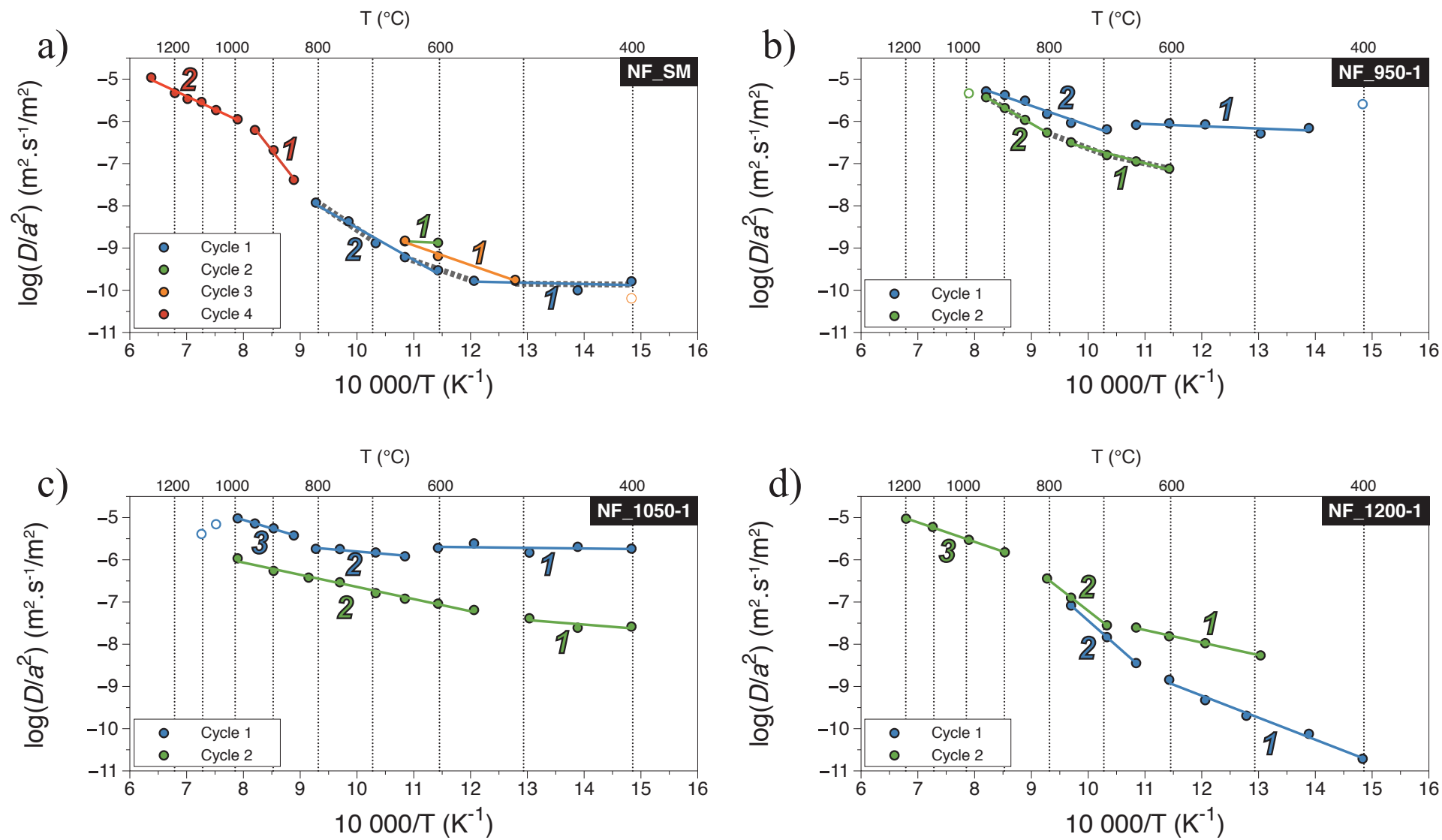


Figure 4

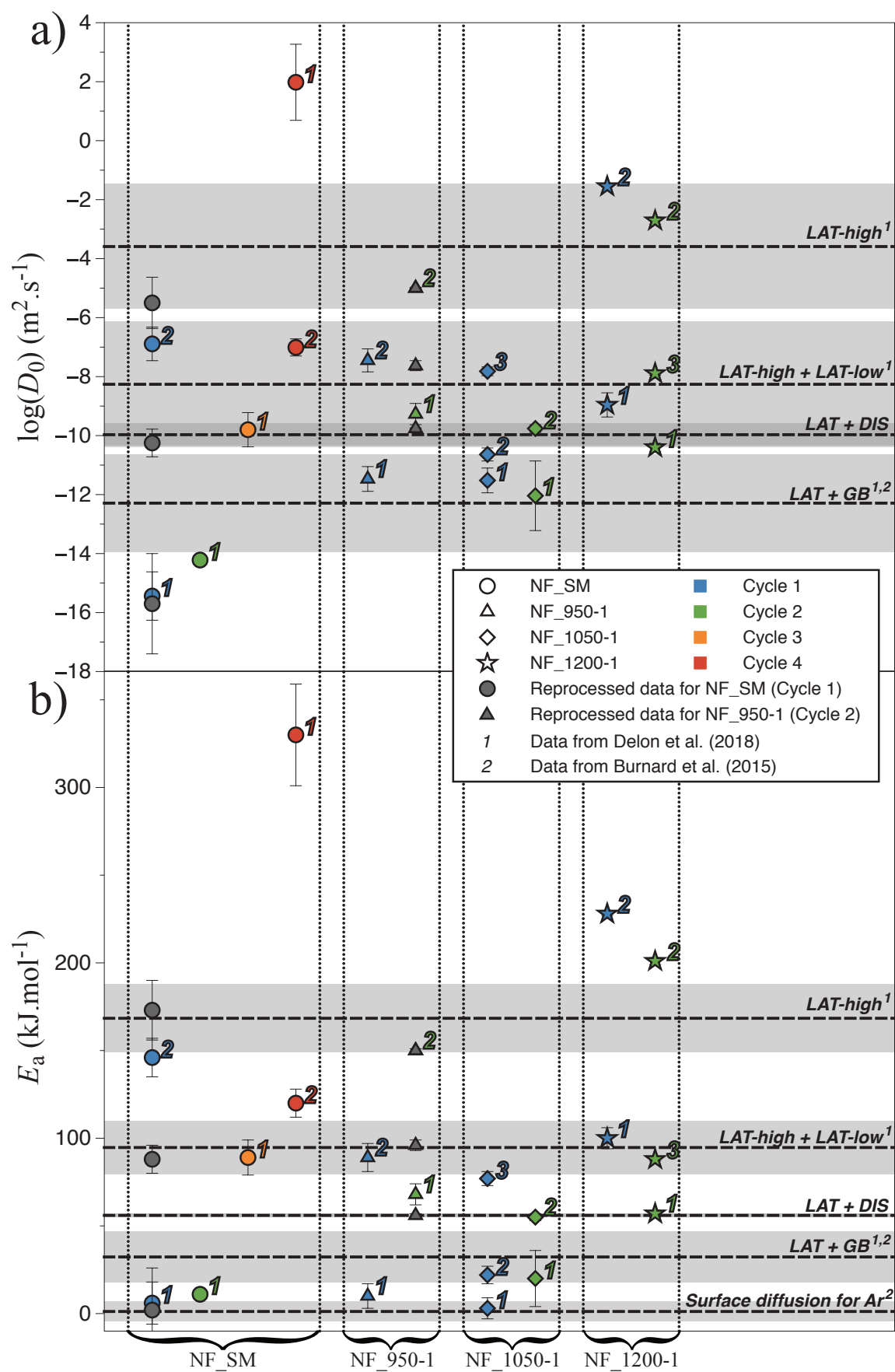


Figure 5

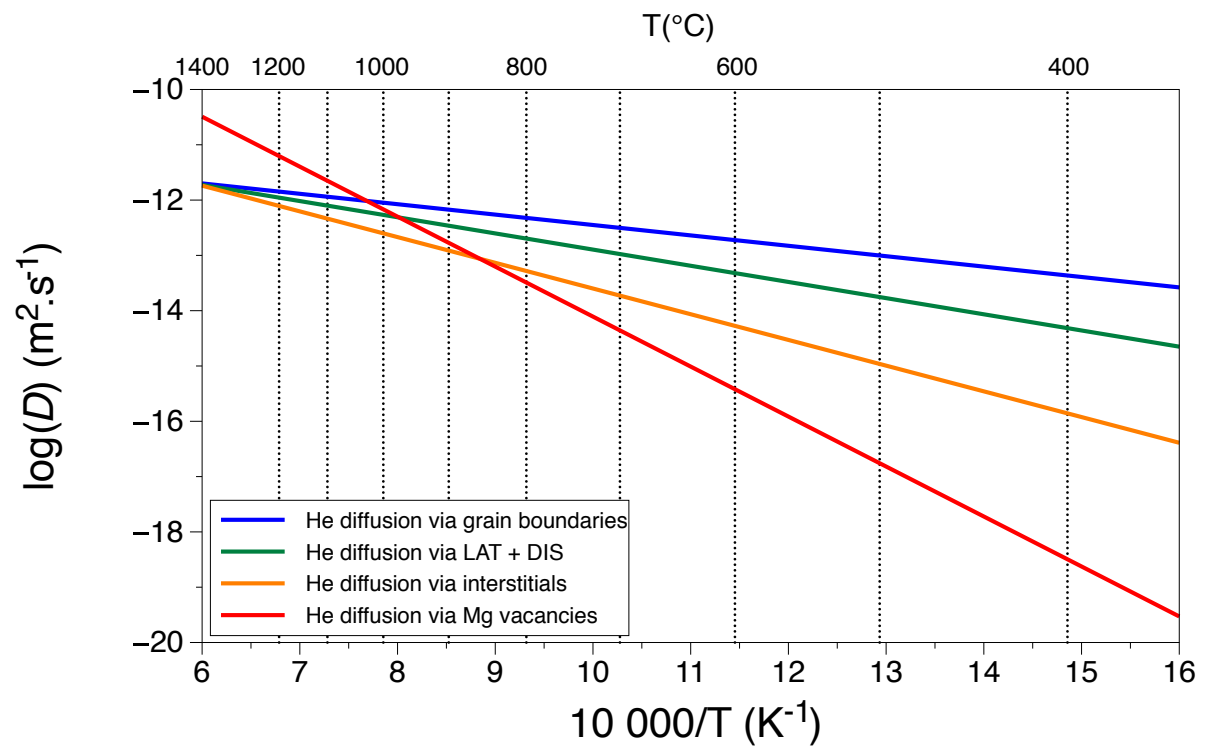


Figure 6

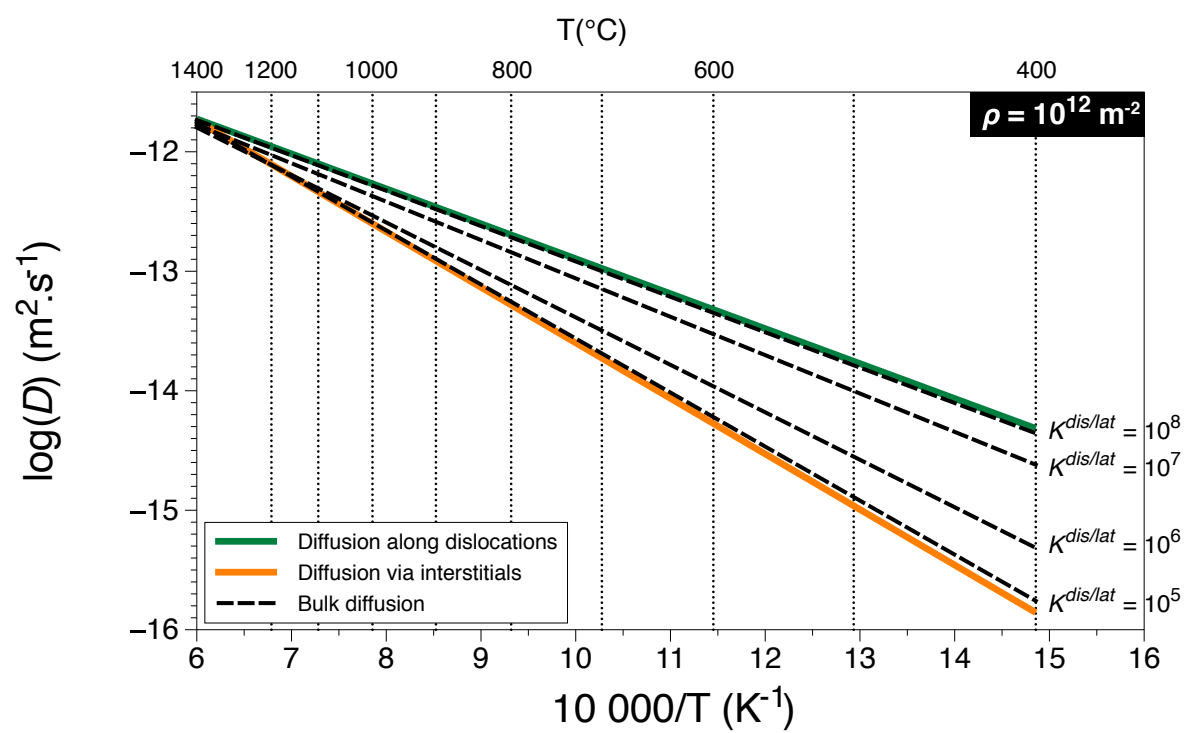


Figure 7